UCB-NE-4222

Long-Term Behavior of Bentonite Buffer in a Geologic Repository for High-Level Wastes

J. Ahn, P. L. Chambré, and J. Verbeke

Department of Nuclear Engineering
University of California
Berkeley, California 94720

May 1999

The authors invite comments and would appreciate being notified of any errors in the report.

Joonhong Ahn
Department of Nuclear Engineering
University of California
Berkeley, CA 94720
USA

ahn@nuc.berkeley.edu

Table of Contents

1 INTRODUCTION 1

2 MATHEMATICAL FORMULATION OF BENTONITE SWELLING IN A CYLINDRICAL FRACTURE BY CONSOLIDATION THEORY 2

2. 1 DERIVATION OF GENERAL GOVERNING EQUATION 2
2. 2 MATHEMATICAL FORMULATION FOR EXPANSION FROM CYLINDRICAL BENTONITE SATURATED WITH WATER 5
2.2.1 Governing equation for void ratio in expanding bentonite 5
2.2.2 Initial and Boundary Conditions 7
2.2.3 Location of bentonite expansion tip 7

3 NUMERICAL SOLUTION SCHEME 9

3. 1 SPATIAL DISCRETIZATION VIA GALERKIN METHOD 9
3. 2 TIME INTEGRATION SCHEME 11
3. 3 INITIALIZATION 16

4 NUMERICAL EVALUATIONS 18

4. 1 INPUT DATA 18
4. 2 VERIFICATION WITH ANALYTICAL SOLUTION FOR CONSTANT COEFFICIENTS 21
4. 3 VALIDATION WITH EXPERIMENTAL RESULTS 27

5 SUMMARY OF ASSUMPTIONS AND LIMITATIONS OF THE MODEL 29

6 CONCLUSIONS 30

7 REFERENCES 31

Appendix: Manual for SABRE4 Code

List of Figures

FIGURE 1 EXPERIMENTAL SETUP BY PNC FOR BENTONITE EXPANSION THROUGH A SIMULATED PLANAR FRACTURE. 1
FIGURE 2 BENTONITE EXPANSION EXPERIMENT. PHOTOS TAKEN FROM THE TOP OF THE SPECIMEN FOR TWO DIFFERENT TIMES (COURTESY: POWER REACTOR AND NUCLEAR FUEL DEVELOPMENT). 1
FIGURE 3 GEOMETRICAL DEFINITION OF THE PROBLEM AND BOUNDARY CONDITIONS. 6
FIGURE 4 MASS FLOW AT THE INNER BOUNDARY AT $R = R(0)$ WHERE THE FRACTURE INTERSECTS WITH THE BULK BENTONITE, AND AT THE OUTER BOUNDARY AT $R = R(T)$. 8
FIGURE 5 RELATIONSHIP BETWEEN THE VOID RATIO AND THE SWELLING PRESSURE. 19
FIGURE 6 THE PERMEABILITY (SOLID AND DASHED LINES) AND THE COMPRESSIBILITY COEFFICIENT (CASES 1, 2, AND 3) OF THE BENTONITE SPECIMEN AS FUNCTIONS OF THE VOID RATIO 20
FIGURE 7 VARIATION OF CEXP(GE) WITH THE VOID RATIO. 20
FIGURE 8 COMPARISON OF NUMERICAL RESULTS OF CASE 2 WITH THE ANLYTICAL SOLUTION (105) 26
FIGURE 9 COMPARISON OF NUMERICAL RESULTS FOR CASES 1, 2, AND 3 FOR DIFFERENT VOID RATIOS AT THE TIP WITH THE EXPERIMENTAL RESULTS 28
FIGURE 10 SPATIAL DISTRIBUTIONS OF THE VOID RATIO IN THE EXPANDING BENTONITE IN THE FRACTURE FOR DIFFERENT TIMES FOR CASE 3. 28

List of Tables

TABLE I DETERMINATION OF THE PERMEABILITY, THE COMPRESSIBILITY COEFFICIENT, COEFFICIENTS C, AND G. 23

1 INTRODUCTION

This report presents results of a numerical analysis for bentonite expansion in a planar fracture. A mathematical model has been developed in this study based on Terzaghi's consolidation theory [1] for clay material. Numerical solutions for the space-time-dependent void ratio in the expanding bentonite are obtained by applying the Finite Element Method. A computer code, SABRE, has been developed for the numerical solutions. The numerical results are validated by the experimental results that were already reported elsewhere [2, 3].

Figure 1 shows the experimental setup used by PNC [2, 3] to study the expansion of bentonite through fractures. A piece of bentonite was confined in a cylindrical non-deformable volume of diameter 50 mm. The bentonite expanded through the horizontal planar gap. The gap had a constant width and was filled up with stagnant water, which had previously been distilled and ion-exchanged. Photographs were taken by a camera just above the bentonite. The pictures were analyzed to measure the radial bentonite expansion as a function of time. Figure 2 shows that bentonite expands through the planar fracture concentrically. The location of the expansion tip in the fracture was observed to be proportional to the square root of the elapsed time.

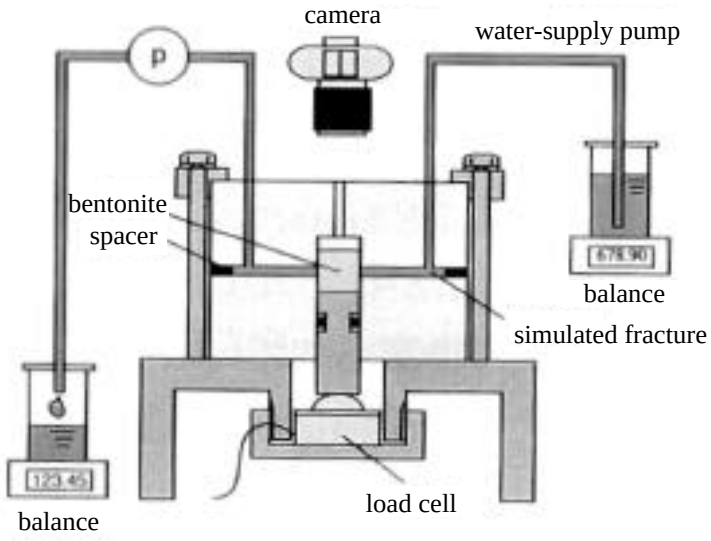

Figure 1 **Experimental setup by PNC for bentonite expansion through a simulated planar fracture.**

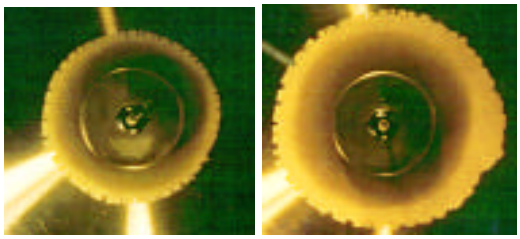

Figure 2 **Bentonite expansion experiment. Photos taken from the top of the specimen for two different times (Courtesy: Power Reactor and Nuclear Fuel Development).**

The objective of this study is to establish a mathematical model that simulates the available experimental results for the bentonite expansion.

In Chapter 2, a mathematical model for bentonite expansion is established for a geometry that simulates the experiment. The physical processes are modeled by formulating the governing equation for the space-time-dependent void ratio, defined as the ratio of the void volume to the solid-phase volume. The water permeability and the compressibility of the bentonite, which are two key parameters for bentonite expansion, are functions of the void ratio. The obtained governing equation is a non-linear diffusion-like equation with void-ratio-dependent coefficients. Simplifications are introduced in order to consider the bentonite expansion in a one-dimensional radial coordinate system, rather than in a full three-dimensional configuration.

In Chapter 3, a numerical solution is obtained for the space-time dependent void ratio by the finite element technique. The model domain has a moving boundary. The finite element solution is combined with a predictor-corrector scheme for evaluations of the void ratio distribution and the location of the moving boundary. A computer code, SABRE, is developed based on the numerical scheme.

In Chapter 4, verification of the code and validation of the model are conducted.

The verification of the numerical scheme developed in Chapter 3 is done by comparing the numerical results with an analytical solution. To obtain the bench-mark analytical solution, a special case of the governing equation is considered, where the coefficients are set constant.

After the code is verified with the analytical solution, validation of the model with the experimental results is performed. Numerical results obtained for the experimental conditions are compared with the experimental results. Since the experiment was performed before the model has been established in this study, not all the parameter values necessary for the model calculation were measured by the experiment. For example, the swelling pressure was measured only for void ratios between 0.3 and 1.0 although it turns out to be in this study that the void ratio dependency for a void ratio greater than 3 is crucial for the expansion speed. For such parameters, parametric surveys have been performed to determine the best fit choices.

It is hoped that the present study will provide partial basis to understand the long-term stability of the engineered barrier system, which include bentonite as a backfill material.

2 MATHEMATICAL FORMULATION OF BENTONITE SWELLING IN A CYLINDRICAL FRACTURE BY CONSOLIDATION THEORY

Microscopically bentonite expansion can be understood as the combined effects of complex interactions of particles, water molecules, and solute ions in water. However, in this study, bentonite expansion in a macroscopic scale, i.e., of the order of a few centimeters to meters, is of particular interest. Since expansion of bentonite occurs due to the existence of water, bentonite expansion can be modeled by analyzing movement of water in the expanding bentonite under the assumption that the deformation of the bentonite solid phase can be handled according to Terzaghi's one-dimensional consolidation theory [1]. For water flow in deformable porous media, a mathematical model was developed by Narashimhan and Witherspoon [4]. In this study, their formulation is adopted. Appropriate initial and boundary conditions are determined in this study to simulate the experimental conditions [2, 3].

2. 1 Derivation of general governing equation

The fundamental equation of transient groundwater motion is a mass conservation equa-

tion [4]. For a flow region which deforms with time, it can be expressed in an integral form as

$$- \int_{\Gamma} \rho_w \vec{q} \cdot \vec{n} d\Gamma = \frac{D}{Dt} \int_{V} \rho_w \theta dV, \tag{1}$$

where ρ_w [kg/m^3] is the water density, θ [dimensionless] the volumetric moisture content, $\vec{q}$ [m/sec] the vector flux density of water relative to the solid particles and *D/Dt* denotes the material derivative. Γ [m^2] and V [m^3] are the boundary and the volume of the domain of interest, respectively. If the volume element is appropriately small so that ρ_w and θ can be treated as average values over V, then (1) becomes

$$- \int_{\Gamma} \rho_w \vec{q} \cdot \vec{n} d\Gamma = \frac{D}{Dt} (\rho_w \theta V). \tag{2}$$

We now introduce Darcy's law [5] for the equation of motion in the form

$$\vec{q} = - \frac{k \rho_w g}{\mu} \vec{\nabla} h, \tag{3}$$

where k [m^2], g [m/sec^2], and μ [kg/m•sec] are the permeability, the gravitational constant, and the viscosity coefficient of water, respectively. h [m] is the total head, and is broken into two components:

$$h = h_e + \frac{p_w}{\gamma_w}, \tag{4}$$

where h_e [m] is the elevation head, p_w [N/m^2] the pore water pressure and $\gamma_w = \rho_w g$ [kg/m^2 sec^2] the specific weight of water.

If we assume that the elevation is fixed during the time interval, $Dh_e/Dt = 0$, and that ρ_w, V, and θ are functions of only p_w, substitution of (3) into (2) leads to

$$\int_{\Gamma} \rho_w \frac{k \rho_w g}{\mu} \vec{\nabla} h \cdot \vec{n} d\Gamma = M_c \frac{D p_w}{Dt}, \tag{5}$$

where

$$M_c = \frac{d}{d p_w} (\rho_w n S V), \tag{6}$$

$$\theta = nS, \tag{7}$$

and n is the porosity [dimensionless]. M_c [m•sec^2] represents the mass of fluid which the volume element V can absorb due to a unit change in the average value of p_w over V. S [dimensionless] is the degree of saturation, defined as the ratio of void volume filled with water to the total void volume. If we assume that water is incompressible, (6) can be calculated as

$$M_c = \rho_w S V_s \frac{de}{d p_w} + \rho_w e V_s \frac{dS}{d p_w}. \tag{8}$$

We note that $nV = V_v = eV_s$, where V_s [m^3] is the volume of the solid phase, constant over time and V_v [m^3] is the void volume. e [dimensionless] is the void ratio, defined as the ratio between the void volume and the solid phase volume.

The first term in the right-hand side of (8) expresses the mass of fluid which V can absorb due to deformation of soil skeleton. According to the Terzaghi's one-dimensional consolidation theory [1], e is a function of effective stress σ' [N/m^2]. σ' in turn is a function of the total head h. The effective stress, σ', is defined in [1] and modified for an unsaturated medium by [6], as

$$\sigma' = \sigma - p_w \chi. \tag{9}$$

The total stress σ [N/m^2] acts over the entire cross-sectional area under consideration (including solid skeleton and voids), and the pore water pressure, p_w, acts over the total area minus the solid-particle contact area. The effective stress is considered to be carried by the solid skeleton of a porous medium. χ is the Bishop's parameter [6], which is to be determined by experiments and has a strong non-linear relation to the saturation S, i.e., $\chi = \chi(S)$, $0 \le \chi \le 1$. χ becomes unity when the medium is saturated with water ($S = 1$).

For the case of bentonite, the total stress is supported by the fluid pressure in the void spaces and the swelling pressure, π [N/m^2], as a net effect of electrical repulsion and attraction between particles, i.e.,

$$\sigma = p_w \chi + \pi . \tag{10}$$

Comparing (9) with (10), we obtain

$$\sigma' = \pi \tag{11}$$

We now make an assumption that is reasonable under most field conditions that the total stress σ at any point in the system does not change in time. Then, the changes in the effective stress (or the swelling pressure by (11)) and the pore water pressure are related by

$$\Delta\sigma' = -\left(\chi \Delta p + p \Delta\chi\right), \tag{12}$$

or

$$\frac{d\sigma'}{dp} = -\chi', \text{ where } \chi' = \chi + p\frac{d\chi}{dp} \tag{13}$$

For a saturated medium, $\chi = 1$, or $\chi' = 1$.

In the light of (13), the first term of the right hand side of (8) becomes

$$\frac{d(nV)}{dp} = -V_s \chi' \frac{de}{d\sigma'}. \tag{14}$$

In soil mechanics literature, it is customary to express stress-strain relationships by plotting e versus σ' or π. Analysis of a large number of uni-axial test data indicates that a plot of e versus log σ' is approximately a straight line [7]. The slope of the best-fitting straight line is called the 'swelling index' C_S [dimensionless], obtained as

$$C_s = -\frac{de}{d\log_{10}\sigma'} = 2.303\sigma' a_v, \tag{15}$$

where

$$a_v = -\frac{de}{d\sigma'}, \text{ the coefficient of compressibility [m}^2\text{/N]}. \tag{16}$$

With (14) and (16), the first term of (8) can be written as

$$\rho_w S\frac{d(nV)}{dp} = \rho_w S V_s a_v \chi' . \tag{17}$$

Substituting (17) into (8) gives the final expression for M_C as

$$M_c = \rho_w V_s\left(S a_v \chi' + e\frac{dS}{dp}\right). \tag{18}$$

Substitution of (18) into (5) yields

$$\frac{1}{V}\int_{\Gamma}\frac{k\rho_w g}{\mu}\vec{\nabla}h\cdot\vec{n}d\Gamma=\frac{1}{1+e}\left(Sa_v\chi'+e\frac{dS}{dp_w}\right)\frac{\partial p_w}{\partial t}. \tag{19}$$

Here, we have assumed that the material derivative is replaced by the partial derivative.

Furthermore, by letting the elemental volume become arbitrarily small, we may write

$$\frac{\rho_w g}{\mu}\nabla\cdot(k\nabla h)=\frac{1}{1+e}\left(Sa_v\chi'+e\frac{dS}{dp_w}\right)\frac{\partial p_w}{\partial t} \tag{20}$$

Equation (20) is the fundamental equation that describes the behavior of a deformable medium with incompressible fluid.

We assume that bentonite is saturated with water, i.e., $S = 1$. Then, (20) reduces to

$$\frac{\rho_w g}{\mu}\nabla\cdot(k\nabla h)=\frac{1}{1+e}\frac{\partial e}{\partial t} \tag{21}$$

Substituting (4) into (21) and assuming the elevation head h_e is constant gives

$$\frac{1}{\mu}\nabla\cdot(k(e)\nabla p_w)=\frac{1}{1+e}\frac{\partial e}{\partial t}. \tag{22}$$

By the chain rule of derivative and using (13) and (16)

$$\frac{\partial p_w}{\partial x}=\frac{dp_w}{d\sigma'}\frac{d\sigma'}{de}\frac{\partial e}{\partial x}=(-1)\left(-\frac{1}{a_v}\right)\frac{\partial e}{\partial x}=\frac{1}{a_v(e)}\frac{\partial e}{\partial x}. \tag{23}$$

Then, (22) can be written in terms of e as

$$\frac{1}{\mu}\nabla\cdot\left(\frac{k(e)}{a_v(e)}\nabla e\right)=\frac{1}{1+e}\frac{\partial e}{\partial t} \tag{24}$$

Equation (24) is the fundamental equation for water flow in water-saturated, deformable media with incompressible fluid. The governing equation (24) is solved in Chapter 3 numerically with appropriate initial and boundary conditions given in the next section. The analytical solution is also obtained for a simplified problem, where the governing equation (24) is reduced to a linear diffusion equation with constant coefficients. The analytical solution is utilized for the verification of the numerical scheme developed in Chapter 3.

2. 2 Mathematical formulation for expansion from cylindrical bentonite saturated with water

2.2.1 Governing equation for void ratio in expanding bentonite

We consider a cylindrical geometry as defined in Figure 3. A water-filled horizontal fracture intersects a water-saturated bulk bentonite of height H and radius $R(0)$. The aperture, L, is assumed the same everywhere in the fracture. Because, in the present model, the bentonite expansion is considered based on the one-dimensional consolidation theory, the effect of fracture apertures resulting from the friction forces between the expanding bentonite and the fracture walls is not taken into account (see discussions in Chapter 5). Thus, the expansion speed is independent of the fracture aperture in the model.

The expansion is considered to occur in the region $R(0) \le r \le R(t)$, where $R(t)$ is the location of the expanding tip in the fracture at time t. (see Figure 3). Water is taken up at the tip.

Water flows through the expanding bentonite between $R(0)$ and $R(t)$, and then eventually flows into the bulk bentonite region through the intersection of the fracture with the bulk bentonite at $r = R(0)$. The water that has just entered the bulk bentonite region causes bentonite swelling. Swollen bentonite will extrude into the fracture, resulting in the advancement of the tip in the fracture.

To simulate this phenomenon, the governing equation (24) must be solved for a three-dimensional space with appropriate side conditions. In this study, to simplify the full three-dimensional configuration, only the region for r between $R(0)$ and $R(t)$ is considered. The bentonite expansion in the fracture is decoupled from the bulk bentonite region by assuming an appropriate boundary condition at the intersection, $r = R(0)$. Then, with radial symmetry assumed for bentonite expansion, the governing equation (24) is to be solved in a one-dimensional cylindrical coordinate system.

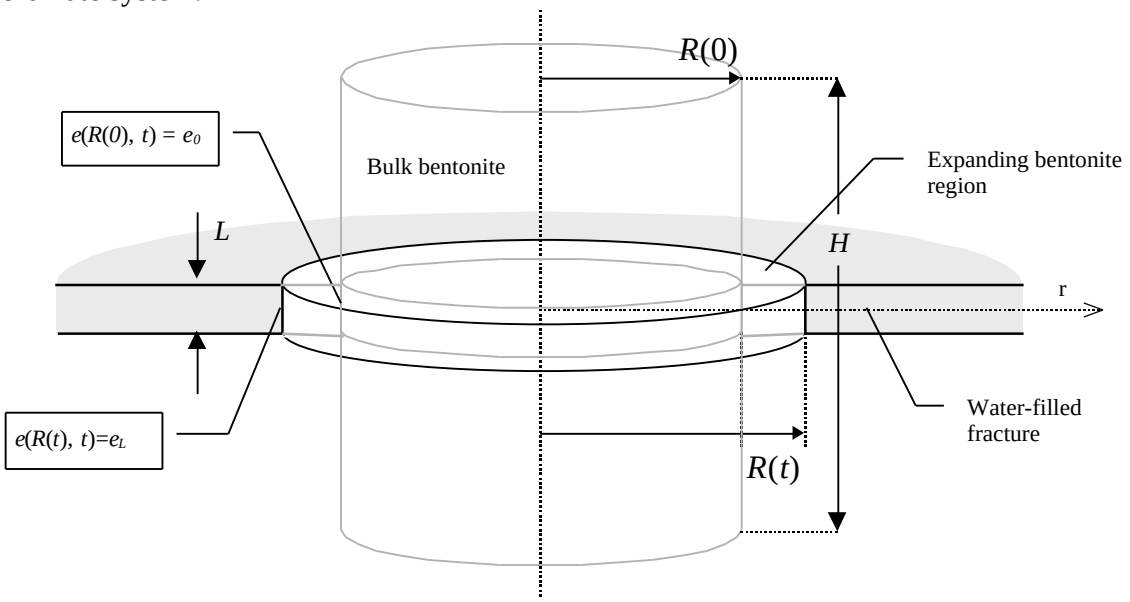

Figure 3 Geometrical definition of the problem and boundary conditions.

The governing equation (24) is written in a cylindrical coordinate system as

$$\frac{1}{1+e}\frac{\partial e}{\partial t} = \frac{1}{r}\frac{\partial}{\partial r}\left[\frac{k(e)}{\mu a_v(e)} r \frac{\partial e}{\partial r}\right]. \tag{25}$$

From (15), the compressibility coefficient, a_v, is expressed as,

$$a_v = \frac{C_s}{2.303\sigma'}. \tag{26}$$

The effective stress, σ', can be approximated in a form of an exponential function as [4]

$$\sigma' = \sigma'_0 \exp\left[-\frac{2.303}{C_s}\left(e - e_0^{\sigma}\right)\right] \tag{27}$$

where σ'_0 and e_0^{σ} represent an arbitrarily chosen point.

With (26) and (27) the compressibility coefficient, a_v, can be written as

$$a_v = \frac{C_s}{2.303\sigma_0'} \exp\left(\frac{2.303}{C_s}\left(e - e_0^{\sigma}\right)\right). \tag{28}$$

We represent the permeability k as an exponential function of e [4]

$$k = k_0 \exp\left(\frac{2.303}{C_k}\left(e - e_0^{k}\right)\right), \tag{29}$$

where C_k [dimensionless] is obtained by fitting the experimental results for e versus $\log k$, with a straight line. k_0 and e_0^k represent an arbitrarily chosen point.

With (28) and (29), the governing equation (25) can be written as

$$\frac{C}{r}\frac{\partial}{\partial r}\left[r\exp(Ge)\frac{\partial e}{\partial r}\right] = \frac{1}{1+e}\frac{\partial e}{\partial t} \quad \text{on } R(0) < r < R(t) \text{ for } t > 0, \tag{30}$$

where C and G are constants determined by

$$\begin{cases} G = 2.303\left(\dfrac{1}{C_k} - \dfrac{1}{C_s}\right) \\ C = \dfrac{2.303\sigma_0' k_0}{\mu C_s}\exp\left[2.303\left(\dfrac{e_0^{\sigma}}{C_s} - \dfrac{e_0^{k}}{C_k}\right)\right] \end{cases} \tag{31}$$

Equations (30) and (31) are the governing equations, for which the numerical scheme is developed in Chapter 3.

2.2.2 Initial and Boundary Conditions

At the time $t = 0$, the properties of the bentonite are homogeneous. The void ratio is assumed to be uniform with e_0 throughout the bulk bentonite:

$$e(r, 0) = e_0 \text{ for } 0 \le r \le R(t). \tag{32}$$

Water is taken up at the tip $R(t)$ and flows in the expanding bentonite in the fracture. At $r = R(0)$, water enters the cylindrical bulk bentonite in the domain $0 \le r \le R(0)$. The water entering this domain causes expansion of the bulk bentonite in the cylinder, and is assumed to be replaced by bentonite extruding into the fracture at $r = R(0)$. (See section 2.2.3 for more details.)

Two boundary conditions are imposed on (30) as shown in Figure 3. The void ratio at the tip $r = R(t)$ is assumed equal to a constant value e_L,

$$e(R(t), t) = e_L \text{ for } t>0. \tag{33}$$

The other boundary condition at $r = R(0)$, we assume the following boundary condition,

$$e(R(0), t) = e_0 \text{ for } t>0. \tag{34}$$

It is assumed that the water volume that has entered the bulk bentonite $0 \le r \le R(0)$ is distributed homogeneously in this domain, and that the average void ratio in this region can be approximated by e_0. This assumption is valid when the volume of water that has entered the domain $0 \le r \le R(0)$ is negligible to the total void volume in the domain. This assumption is checked by the numerical evaluations in Section 4.3.

2.2.3 Location of bentonite expansion tip

The volume $V(t)$ of the domain $R(0) \le r \le R(t)$ consists of time-dependent volumes of

solid and water phases, $V_s(t)$ and $V_w(t)$, respectively. The rate of change of the water mass in the domain is expressed as $\frac{d}{dt}\left(\rho_w V_w(t)\right)$. This can be equated to the net mass flow rate through the two boundaries at $r = R(t)$ and $r = R(0)$.

First, only water enters through the boundary at $r = R(t)$ (see Figure 4). The mass flow rate of water through the boundary at $r = R(t)$ is equal to $-2\pi R(t) L \rho_w \vec{q}\vec{n}\big|_{r=R(t)}$, where $\vec{q}$ is the Darcy flux, defined by (8), and $\vec{n}$ is a unit vector outward normal to the boundary. $\vec{q}\vec{n}$ is positive if the mass flow takes place in the outward direction at the boundary of interest. Thus, the minus sign is included in this case.

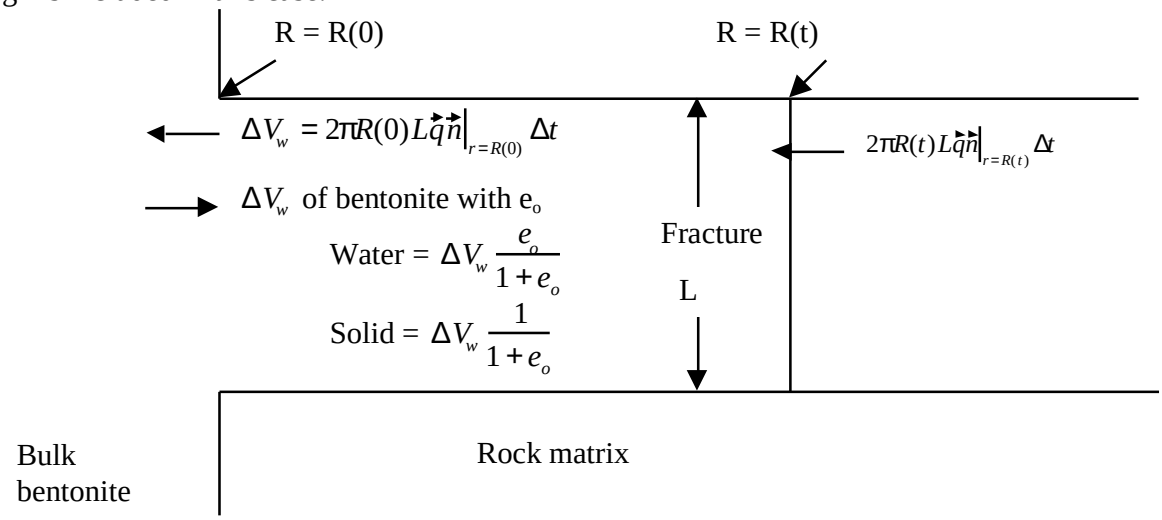

Figure 4 Mass flow at the inner boundary at $r = R(0)$ where the fracture intersects with the bulk bentonite, and at the outer boundary at $r = R(t)$.

The mass flow of water through $r = R(0)$ is less intuitive to compute. The volume of water $\Delta V_w(t)$ crossing the boundary at $r = R(0)$ from the fracture to the bulk bentonite during the time interval Δt is expressed as $\Delta V_w(t) = 2\pi R(0) L \vec{q}\vec{n}\big|_{r=R(0)} \Delta t$ (see Figure 4). In return, the identical volume $\Delta V_w(t)$ of bentonite with a void ratio of e_0 is assumed to be added to the fracture during the same time interval Δt through the boundary at $r = R(0)$. The bentonite added to the fracture contains both solid and water phases with a void ratio of e_0. The water volume added to the fracture through the boundary at $r = R(0)$ is obtained as $\frac{e_0}{1+e_0}\Delta V_w$. Considering the two contributions, the net volume of water lost through the surface $r = R(0)$ during Δt is equal to $\frac{1}{1+e_0}\Delta V_w$.

Then, the mass conservation equation for water for the domain $R(0) \le r \le R(t)$ is obtained as

$$\frac{d}{dt}\left(\rho_w V_w(t)\right) = -\frac{1}{1+e_0} 2\pi R(0) L \rho_w \vec{q}\vec{n}\big|_{r=R(0)} + \left\{-2\pi R(t) L \rho_w \vec{q}\vec{n}\big|_{r=R(t)}\right\}. \quad (35)$$

The first term in the right hand side represents the water volume lost at the inner boundary, whereas the second term including the minus sign represents the water volume gained at the outer boundary.

Substituting

$$V_w(t) = V(t) - V_s(t), \tag{36}$$

and dividing (35) by ρ_w, we get

$$\frac{dV(t)}{dt} - \frac{dV_s(t)}{dt} = -\frac{1}{1+e_0} 2\pi R(0) L \vec{q}\vec{n}\Big|_{r=R(0)} - 2\pi R(t) L \vec{q}\vec{n}\Big|_{r=R(t)} \tag{37}$$

The volume of the solid phase added to the domain during the time interval Δt is $\frac{1}{1+e_0} 2\pi R(0) L \vec{q}\vec{n}\Big|_{r=R(0)} \Delta t$. Substituting this into (37) yields

$$\frac{dV(t)}{dt} = -2\pi R(t) L \vec{q}\vec{n}\Big|_{r=R(t)}. \tag{38}$$

With

$$V(t) = \pi\left(R^2(t) - R^2(0)\right)L, \tag{39}$$

(38) is written as

$$\frac{dR(t)}{dt} = \frac{k(e)}{\mu a_v(e)} \frac{\partial e}{\partial r}\Big|_{r=R(t)} \quad \text{for } t > 0, \tag{40}$$

which is the fundamental equation describing the expansion of a cylindrical volume of a saturated medium contacted with water.

On substitution of (28) and (29), (40) becomes

$$\frac{dR(t)}{dt} = C\exp\left(Ge(R(t),t)\right)\frac{\partial e}{\partial r}\Big|_{r=R(t)} \quad \text{for } t > 0. \tag{41}$$

(41) will be used for the numerical scheme development in Chapter 3.

3 NUMERICAL SOLUTION SCHEME

In this Chapter, numerical solutions for (30) and (41) and a scheme to calculate *e(r,t)* numerically are established. The basic algorithm is based on a fully implicit Galerkin/Finite Element technique on deforming elements combined with a predictor-corrector scheme. By combination of the predictor and the corrector, the temporal accuracy can be controlled by automatic time step modification.

3. 1 Spatial discretization via Galerkin method

The finite element spatial discretization of equation (30) is performed via the Galerkin method, wherein the void ratio *e(r,t)* is approximated by a sum of *N* shape functions $\varphi_k(r)$ weighted by *N* nodal values $e_k(t)$:

$$\tilde{e}(r,t) = \sum_{k=1}^{N} e_k(t)\varphi_k(r) \text{ on } R(0) \le r \le R(t), \text{ for } t>0, \tag{42}$$

where $\tilde{e}(r,t)$ denotes a finite-element approximation of $e(r,t)$.

The approximation, $\tilde{e}(r,t)$, is determined in such a way that $\tilde{e}(r,t)$ satisfies the following

equation,

$$\int_{R(0)}^{R(t)} \varphi_i \left[C \frac{\partial}{\partial r} \left(r \exp(G\tilde{e}) \frac{d\varphi_k}{dr} \right) e_k \right] 2\pi r dr = \int_{R(0)}^{R(t)} \varphi_i \left[\frac{1}{1+\tilde{e}} \frac{de_k}{dt} \varphi_k \right] 2\pi r dr, \; t > 0, \tag{43}$$

where the equations are set for $i = 1, 2, \ldots, N$.

By integration by parts of the left hand side,

$$\left[\int_{R(0)}^{R(t)} \varphi_i \frac{1}{1+\tilde{e}} \varphi_k r dr \right] \dot{e}_k + \left[\int_{R(0)}^{R(t)} Cr \exp(G\tilde{e}) \frac{d\varphi_i}{dr} \frac{d\varphi_k}{dr} dr \right] e_k = \left[C\varphi_i r \exp(G\tilde{e}) \frac{d\varphi_k}{dr} e_k \right]_{r=R(0)}^{r=R(t)},$$

$$t > 0, \; i = 1, 2, \ldots, N, \tag{44}$$

where the dot symbol denotes the derivative with respect to time.

Equation (44) is a system of non-linear, first-order ordinary differential equations in time, which can be written in the following compact matrix form:

$$\underline{\underline{M}}(t)\dot{\underline{e}}(t) + \underline{\underline{K}}(t)\underline{e}(t) = \underline{F}(t) \tag{45}$$

where

$$\begin{cases} M_{ik}(\underline{e}) = \displaystyle\int_{R(0)}^{R(t)} \varphi_i \frac{1}{1+\tilde{e}} \varphi_k r dr \\ K_{ik}(\underline{e}) = \displaystyle\int_{R(0)}^{R(t)} Cr \exp(G\tilde{e}) \frac{d\varphi_i}{dr} \frac{d\varphi_k}{dr} dr \\ F_i(\underline{e}) = \left[C\varphi_i r \exp(G\tilde{e}) \frac{d\varphi_k}{dr} e_k \right]_{r=R(0)}^{r=R(t)} \end{cases} . \tag{46}$$

$\underline{e}(t)$ is the nodal value vector composed of the nodal values $e_k(t)$, $k = 1, 2, \ldots, N$, of the finite-element approximation of the void ratio.

From (41) and (42), the motion of the moving boundary is determined by

$$\dot{R} = C \exp(G\tilde{e}) \left. \frac{d\varphi_k}{dr} \right|_{r=R(t)} e_k \text{ for } t>0. \tag{47}$$

Equations (45) and (47) are the set of first-order differential equations to solve.

The internal node positions must be redefined because at every time step the domain increases. We use the following simple law for the location of node m:

$$r_m(t) = R(0) + c_m R(t) \text{ for } t>0, \tag{48}$$

where c_m are constants, $m = 1, 2, \ldots, N$.

We use linear shape functions:

$$\varphi_k(r) = \begin{cases} \dfrac{r - r_{k-1}}{r_k - r_{k-1}}, & r \in [r_{k-1}; r_k] \\ \dfrac{r_{k+1} - r}{r_{k+1} - r_k}, & \textit{for} \quad r \in [r_k; r_{k+1}]. \\ 0, & \textit{otherwise} \end{cases} \tag{49}$$

With these shape functions, the terms of the matrices M_{ik} and K_{ik} in (45) are different from 0 only for $k = i$-1, $k = i$ and $k = i$+1. Concerning the right-hand side of (45), F_i, they are different

from zero only for the extreme terms $i = 1$, and N. The system of equations (45) becomes tridiagonal:

$$\begin{bmatrix} M_{11} & M_{12} & 0 & \cdots & 0 & 0 \\ M_{21} & M_{22} & M_{23} & \cdots & 0 & 0 \\ 0 & M_{32} & M_{33} & \cdots & 0 & 0 \\ \vdots & \vdots & \vdots & \ddots & \vdots & \vdots \\ 0 & 0 & 0 & \cdots & M_{NN-1} & M_{NN} \end{bmatrix} \begin{bmatrix} \dot{e}_1 \\ \dot{e}_2 \\ \dot{e}_3 \\ \vdots \\ \dot{e}_N \end{bmatrix} + \begin{bmatrix} K_{11} & K_{12} & 0 & \cdots & 0 & 0 \\ K_{21} & K_{22} & K_{23} & \cdots & 0 & 0 \\ 0 & K_{32} & K_{33} & \cdots & 0 & 0 \\ \vdots & \vdots & \vdots & \ddots & \vdots & \vdots \\ 0 & 0 & 0 & \cdots & K_{NN-1} & K_{NN} \end{bmatrix} \begin{bmatrix} e_1 \\ e_2 \\ e_3 \\ \vdots \\ e_N \end{bmatrix} = \begin{bmatrix} F_1 \\ 0 \\ 0 \\ \vdots \\ F_N \end{bmatrix} \tag{50}$$

and the equation for the motion of the boundary condition (47) reads :

$$\dot{R} = C\exp\left(Ge_N\right)\left[\left.\frac{d\varphi_{N-1}}{dr}\right|_{r=R(t)} e_{N-1} + \left.\frac{d\varphi_N}{dr}\right|_{r=R(t)} e_N\right] \text{ for } t>0. \tag{51}$$

3. 2 Time integration scheme

We solve (45) and (47) in a decoupled fashion. We consider here implicit methods because of their greater stability. This greater stability exacts a significant computational price, since the solution of the system of equations must be obtained once per time step.

The integration scheme developed here is based on two second-order-accurate integration techniques proposed by Gresho *et al.* [8], the explicit Adams-Bashforth formula and the implicit trapezoid rule. By combination of these common techniques, a stable scheme is obtained in which the temporal accuracy is controlled by automatic time step modification based on a good estimate of the local single step time truncation error. This automatic time step modification provides a cost-effective algorithm in the sense that the time step is increased whenever possible and decreased only when necessary. The non-linear systems obtained are solved using a Newton-Raphson method, which requires the construction of a linear system. This unsymmetrical linear system is solved via Gaussian elimination.

The overall time integration scheme can be described as follows. From the knowledge of the moving boundary position and the void ratio at time t_n, we predict the moving boundary position and the void ratio at time t_{n+1}. We then solve (45) in the predicted domain, and finally, correct the moving boundary position by solving (47). More precisely, let $\underline{e}^n$ and R^n be the nodal vector of the void ratio and position of the moving boundary at the time t_n:

$$\underline{e}^n = \underline{e}(t_n) \tag{52}$$

$$R^n = R\left(t_n\right) \tag{53}$$

We obtain the corresponding vector and position at time $t_{n+1}=t_n+\Delta t_n$ after completion of the following steps (a) through (f):

(a) Predictor step

We predict $\underline{e}_{pred}$ and R_{pred} at the time t_{n+1} by means of the variable-step, second-order Adams-Bashforth formula:

$$\underline{e}_{pred}^{n+1} = \underline{e}^n + \frac{\Delta t_n}{2}\left[\left(2 + \frac{\Delta t_n}{\Delta t_{n-1}}\right)\dot{\underline{e}}^n - \frac{\Delta t_n}{\Delta t_{n-1}}\dot{\underline{e}}^{n-1}\right], \tag{54}$$

$$R_{pred}^{n+1} = R^n + \frac{\Delta t_n}{2}\left[2 + \frac{\Delta t_n}{\Delta t_{n-1}}\right]\dot{R}^n - \frac{\Delta t_n}{\Delta t_{n-1}}\dot{R}^{n-1}, \tag{55}$$

where the time derivatives $\dot{\underline{e}}^n$, $\dot{\underline{e}}^{n-1}$, $\dot{R}^n$ and $\dot{R}^{n-1}$ are known from the previous time steps, and $\Delta t_n = t_{n+1} - t_n$.

This predictor step performs two important functions: it provides a very good predictor for the trapezoid rule, which contributes substantially to the success of the Newton-Raphson method, and it permits control of the local error. This predictor is thus quite cost-effective.

(b) Relocation of the internal nodes

Relocation of the internal nodes by means of the predicted tip position (55) and the law of motion (48).

(c) Corrector step

Computation of $\underline{e}^{n+1}$ on the predicted finite-element grid by means of the completely stable implicit trapezoid rule. Applied to $\dot{y} = f$, it gives

$$y^{n+1} = y^n + \frac{\Delta t_n}{2}\left(f_n + f_{n+1}\right). \tag{56}$$

In order to apply the implicit trapezoidal rule to discretize (45) in time, we have to assume that $\underline{\underline{M}}$ is invertible at all times t>0. Equation (45) can then be rewritten as

$$\dot{\underline{e}} = \underline{\underline{M}}^{-1}\left(\underline{F} - \underline{\underline{K}}\,\underline{e}\right), \tag{57}$$

and the numerical scheme (56) reads then

$$\underline{e}^{n+1} = \underline{e}^n + \frac{\Delta t_n}{2}\left\{\dot{\underline{e}}^n + \underline{\underline{M}}\left(\underline{e}^{n+1}\right)^{-1}\underline{F}\left(\underline{e}^{n+1}\right) - \underline{\underline{M}}\left(\underline{e}^{n+1}\right)^{-1}\underline{\underline{K}}\left(\underline{e}^{n+1}\right)\underline{e}^{n+1}\right\}. \tag{58}$$

Multiplying by $2/\Delta t_n \underline{\underline{M}}(e^{n+1})$, this equation can be rewritten as a set of algebraic equations in terms of the unknown nodal value vector $\underline{e}^{n+1}$:

$$\left[\frac{2}{\Delta t_n}\underline{\underline{M}}\left(\underline{e}^{n+1}\right) + \underline{\underline{K}}\left(\underline{e}^{n+1}\right)\right]\underline{e}^{n+1} = \left[\underline{\underline{M}}\left(\underline{e}^{n+1}\right)\left(\frac{2}{\Delta t_n}\underline{e}^n + \dot{\underline{e}}^n\right) + \underline{F}\left(\underline{e}^{n+1}\right)\right], \tag{59}$$

where the time derivative $\dot{\underline{e}}^n$ of the nodal value vector and the nodal value vector at the previous time step is used. The integrals in the matrices $\underline{\underline{M}}$, $\underline{\underline{K}}$ and vector $\underline{F}$ are evaluated on the predicted domain $R(0) \le r \le R_{pred}^{n+1}$.

We recognize equation (59) as a nonlinear algebraic system $\underline{\underline{A}}(\underline{x})\underline{x} = \underline{b}(\underline{x})$. We solve it by the Newton-Raphson iterative technique with predicted values of *e* and *R* as first estimates. This method is powerful in time-dependent problems because good first guesses are always available, especially when it is coupled with a predictor equation. The use of predicted values as first estimates in the iterative process is so efficient that a single iteration of Newton-Raphson method is usually sufficient for achieving full convergence.

Newton-Raphson requires the construction of a linear system. In the case of $A_{ij}(\underline{x})x_j - b_i(\underline{x}) = 0$, where a predictor $\underline{x}_{pred}$ is available for the vector $\underline{x}$, the linear system of equations reads:

$$A_{ij}\left(\underline{x}_{pred}\right)x_{j,pred} - b_i\left(\underline{x}_{pred}\right) + \frac{d}{dx_j}\left[A_{ik}(\underline{x})x_{k,pred} - b_i(\underline{x})\right]\Big|_{\underline{x}=\underline{x}_{pred}}\left(x_j - x_{j,pred}\right) = 0, \tag{60}$$

or
$$J_{ij}\left(\underline{x}_{pred}\right)\left(x_j - x_{j,pred}\right) = b_i\left(\underline{x}_{pred}\right) - A_{ij}\left(\underline{x}_{pred}\right)x_{j,pred}, \tag{61}$$

where x_j are the unknowns, $j = 1, 2, \ldots, N$, and $J_{ij}(\underline{x})$ is the Jacobian matrix of $A_{ik}(\underline{x})x_k - b_i(\underline{x})$, $1 \le i \le N$.

The system of equations (61) is commonly solved for $\Delta x_j = x_j - x_{j,pred}$, $j = 1, 2, \ldots, N$. The values x_j are then computed as $x_j = x_{j,pred} + \Delta x_j$. The Jacobian matrix has to be evaluated for $\underline{x} = \underline{x}_{pred}$. We thus have

$$J_{ij}\left(\underline{x}_{pred}\right) = A_{ij}\left(\underline{x}_{pred}\right) + \frac{dA_{ik}(\underline{x})}{dx_j}\,x_{k,pred}\bigg|_{\underline{x}=\underline{x}_{pred}} - \frac{db_i(\underline{x})}{dx_j}\bigg|_{\underline{x}=\underline{x}_{pred}}, \; i, j = 1, 2, \ldots, N. \tag{62}$$

In the case of the system of equations (59), we have to determine the unknown vector $\underline{e}^{n+1}$. The matrix $\underline{\underline{A}}$ and vector $\underline{b}$ read respectively,

$$A_{ij} = \frac{2}{\Delta t_n} M_{ij}\left(\underline{e}^{n+1}\right) + K_{ij}\left(\underline{e}^{n+1}\right), \tag{63}$$

and
$$b_i = M_{ij}\left(\underline{e}^{n+1}\right)\left(\frac{2}{\Delta t_n} e_j^n + \dot{e}_j^n\right) + F_i\left(\underline{e}^{n+1}\right). \tag{64}$$

The Jacobian $\underline{\underline{J}}$ reads thus in our case by grouping terms,

$$\begin{aligned} J_{ij}\left(\underline{e}_{pred}^{n+1}\right) = {} & \frac{2}{\Delta t_n} M_{ij}\left(\underline{e}_{pred}^{n+1}\right) + K_{ij}\left(\underline{e}_{pred}^{n+1}\right) + \frac{2}{\Delta t_n}\frac{d}{de_j^{n+1}} M_{ik}\left(\underline{e}^{n+1}\right)\bigg|_{\underline{e}^{n+1}=\underline{e}_{pred}^{n+1}} \left(e_{k,pred}^{n+1} - e_k^n - \frac{\Delta t_n}{2}\dot{e}_k^n\right) \\ & + \frac{d}{de_j^{n+1}} K_{ij}\left(\underline{e}^{n+1}\right)\bigg|_{\underline{e}^{n+1}=\underline{e}_{pred}^{n+1}} e_{k,pred}^{n+1} - \frac{d}{de_j^{n+1}} F_i\left(\underline{e}^{n+1}\right)\bigg|_{\underline{e}^{n+1}=\underline{e}_{pred}^{n+1}} \end{aligned} \tag{65}$$

The system of equations (59) can thus be written as

$$\begin{aligned} & \left[\frac{2}{\Delta t_n} M_{ij}\left(\underline{e}_{pred}^{n+1}\right) + K_{ij}\left(\underline{e}_{pred}^{n+1}\right) - \frac{2}{\Delta t_n} L_{ij}\left(\underline{e}_{pred}^{n+1}\right) + N_{ij}\left(\underline{e}_{pred}^{n+1}\right) - \frac{\partial F_i\left(\underline{e}^{n+1}\right)}{\partial e_j^{n+1}}\bigg|_{\underline{e}=\underline{e}_{pred}^{n+1}}\right]\left[e_j^{n+1} - e_{j,pred}^{n+1}\right] \\ & = \left[M_{ij}\left(\underline{e}_{pred}^{n+1}\right)\left(\frac{2}{\Delta t_n} e_j^n + \dot{e}_j^n\right) + F_i\left(\underline{e}_{pred}^{n+1}\right)\right] - \left[\frac{2}{\Delta t_n} M_{ij}\left(\underline{e}_{pred}^{n+1}\right) + K_{ij}\left(\underline{e}_{pred}^{n+1}\right)\right] e_{j,pred}^{n+1} \end{aligned} \tag{66}$$

where $i = 1, 2, \ldots, N$, and

$$\begin{cases} L_{ij}\left(\underline{e}_{pred}^{n+1}\right) = \displaystyle\int_{R(0)}^{R(t_{n+1})} \varphi_i \frac{r}{\left(1+\tilde{e}_{pred}^{n+1}\right)^2}\varphi_j\varphi_k dr\left(e_{k,pred}^{n+1} - e_k^n - \frac{\Delta t_n}{2}\dot{e}_k^n\right) \\ N_{ij}\left(\underline{e}_{pred}^{n+1}\right) = \displaystyle\int_{R(0)}^{R(t_{n+1})} \frac{d\varphi_i}{dr} CrG\varphi_j \exp\left(G\tilde{e}_{pred}^{n+1}\right)\frac{d\varphi_k}{dr} dr e_{k,pred}^{n+1} \\ F_i\left(\underline{e}_{pred}^{n+1}\right) = \left[C\varphi_i r \exp\left(G\tilde{e}_{pred}^{n+1}\right)\frac{d\varphi_k}{dr} e_{k,pred}^{n+1}\right]_{r=R(0)}^{r=R(t_{n+1})} \end{cases}. \tag{67}$$

The elements of the matrices $\underline{\underline{K}}$, $\underline{\underline{L}}$, $\underline{\underline{M}}$, $\underline{\underline{N}}$ are different from zero only for $j = i-1$, $j = i$ and j

= i+1. Concerning the vector $\underline{F}$, its elements are different from zero only for i = 1, and N.

Since the boundary conditions (33) and (34) impose the values of the last and first nodal value e_N and e_0, the predictors, $e_{N,pred}^{n+1}$ and $e_{1,pred}^{n+1}$ are set equal to e_L and e_o, respectively. $e_N^{n+1} - e_{N,pred}^{n+1}$ and $e_1^{n+1} - e_{1,pred}^{n+1}$ are set equal to zero for the solution of the system of N equations and N unknowns (66). Using these equalities, this system can be reduced to a system of N-2 equations for N-2 unknowns by removing the first and last lines *(i = 1 and N)* and first and last columns *(j = 1 and N)* of the Jacobian $\underline{J}$ and the first and last elements *(i = 1 and N)* of the right-hand side of (66). Thus, neither $\underline{F}$ nor its derivatives with respect to e_j^{n+1} have to be computed.

The solution of the reduced system usually does not require more than one iteration. However, if the user-specified convergence criterion on the nodal values of the void ratio is not reached after one iteration, we proceed to subsequent iterations. In this case, the matrices $\underline{K}$, $\underline{L}$, $\underline{M}$, $\underline{N}$ in (66) are recalculated on the same spatial domain but with the most recent $\underline{e}^{n+1}$ instead of $\underline{e}_{pred}^{n+1}$.

(d) Correction of the moving boundary position

We correct the moving boundary position R with the void ratio nodal vector $\underline{e}^{n+1}$ found in step (c). Applying the trapezoid rule, the time discretization of (51) leads to

$$R^{n+1} = R^n + \frac{\Delta t_n}{2}\left[C\exp\left(G\tilde{e}^n\right)\frac{d\varphi_k}{dr}\bigg|_{r=R(t_n)} e_k^n + C\exp\left(G\tilde{e}^{n+1}\right)\frac{d\varphi_k}{dr}\bigg|_{r=R(t_{n+1})} e_k^{n+1}\right] \tag{68}$$

The relative difference between the previous and new tip positions R^n and R^{n+1} respectively may be larger than the user-specified convergence criterion. In this case, subsequent iterations through (b), (c) and (d) are necessary. For step (b), the most recent tip position R^{n+1} is used to relocate the internal nodes. Then, the matrices $\underline{K}$, $\underline{L}$, $\underline{M}$, $\underline{N}$ in (66) are recalculated on the new spatial domain *[R(0), R^{n+1}]* instead of *[R(0), R_{pred}^{n+1}]* with the second most recent $\underline{e}^{n+1}$ instead of $\underline{e}_{pred}^{n+1}$. Afterwards, "inner"-iterations are performed on (66) to solve for $\underline{e}^{n+1}$ in step (c) and the tip position is corrected in step (d). These "outer"-iterations are performed until the user-specified convergence criterion on the tip position is fulfilled.

(e) Evaluation of the time derivatives

The time derivatives to be used in step (a) at the next time step have to be evaluated. This is conveniently done by inversion of the trapezoid rule:

$$\dot{\underline{e}}^{n+1} = \frac{2}{\Delta t_n}\left(\underline{e}^{n+1} - \underline{e}^n\right) - \dot{\underline{e}}^n, \tag{69}$$

$$\dot{R}^{n+1} = \frac{2}{\Delta t_n}\left(R^{n+1} - R^n\right) - \dot{R}^n. \tag{70}$$

where $\dot{\underline{e}}^n$ is available from the previous application of the same equation.

(f) Computation of the next time step

An automatic selection of the time increment is made during the simulation, on the basis of the difference between the predicted and corrected values and user-specified level of local time truncation error. The estimation of the local time truncation error begins with a Taylor series analysis of both predictor and corrector schemes. Denoting $y(t_n)$ the exact solution at time t_n and assuming that the exact solution is known at the beginning of the time step, i.e. $y^n=y(t_n)$, we have the following error estimate for the predictor :

$$
\begin{aligned}
& y_{pred}^{n+1} - y\left(t_{n+1}\right) \\
& = y^n + \frac{\Delta t_n}{2}\left(2 + \frac{\Delta t_n}{\Delta t_{n-1}}\right)\dot{y}^n - \frac{\Delta t_n}{\Delta t_{n-1}}\dot{y}^{n-1} - \left(y^n + \Delta t_n \dot{y}^n + \frac{\Delta t_n^{\,2}}{2}\ddot{y}^n + \frac{\Delta t_n^{\,3}}{6}\dddot{y}^n + O\left(\Delta t_n^{\,4}\right)\right) \\
& = -\frac{\Delta t_n^{\,3}}{6}\dddot{y}^n + \frac{\Delta t_n^{\,2}}{2}\left(\dot{y}^n - \dot{y}^{n-1}\right)\frac{1}{\Delta t_{n-1}} - \frac{\Delta t_n^{\,2}}{2}\ddot{y}^n + O\left(\Delta t_n^{\,4}\right)
\end{aligned}
\tag{71}
$$

Introducing the following Taylor series

$$
\dot{y}^n = \dot{y}^{n-1} + \Delta t_{n-1}\ddot{y}^{n-1} + \frac{\Delta t_{n-1}^{\,2}}{2}\dddot{y}^{n-1} + O\left(\Delta t_{n-1}^{3}\right), \tag{72}
$$

the second term of the right-hand side of (71) can be modified using

$$
\left(\dot{y}^n - \dot{y}^{n-1}\right)\frac{1}{\Delta t_{n-1}} = \ddot{y}^{n-1} + \frac{\Delta t_{n-1}}{2}\dddot{y}^{n-1} + O\left(\Delta t_{n-1}^{2}\right). \tag{73}
$$

Replacing the second and third derivatives of *y* with respect to time in (73) by their Taylor series, equation (73) reads now

$$
\begin{aligned}
\frac{\dot{y}^n - \dot{y}^{n-1}}{\Delta t_{n-1}} &= \left(\ddot{y}^n - \Delta t_{n-1}\dddot{y}^n + O\left(\Delta t_{n-1}^{2}\right)\right) + \frac{\Delta t_{n-1}}{2}\left(\dddot{y}^n + O\left(\Delta t_{n-1}\right)\right) + O\left(\Delta t_{n-1}^{2}\right) \\
&= \ddot{y}^n - \frac{\Delta t_{n-1}}{2}\dddot{y}^n + O\left(\Delta t_{n-1}^{2}\right)
\end{aligned}
\tag{74}
$$

The truncation error (71) for the predictor becomes then

$$
y_{pred}^{n+1} - y\left(t_{n+1}\right) = -\frac{1}{12}\left(2 + 3\frac{\Delta t_{n-1}}{\Delta t_n}\right)\Delta t_n^{\,3}\dddot{y}^n + O\left(\Delta t_n^{\,4}\right). \tag{75}
$$

Concerning the corrector step, we have

$$
\begin{aligned}
y_{n+1} - y\left(t_{n+1}\right) &= y^n + \frac{\Delta t_n}{2}\left(\dot{y}^n + \dot{y}^{n+1}\right) - \left(y^n + \Delta t_n \dot{y}^n + \frac{\Delta t_n^{\,2}}{2}\ddot{y}^n + \frac{\Delta t_n^{\,3}}{6}\dddot{y}^n + O\left(\Delta t_n^{\,4}\right)\right) \\
&= \frac{\Delta t_n}{2}\left(\dot{y}^{n+1} - \dot{y}^n\right) - \frac{\Delta t_n^{\,2}}{2}\ddot{y}^n - \frac{\Delta t_n^{\,3}}{6}\dddot{y}^n + O\left(\Delta t_n^{\,4}\right).
\end{aligned}
\tag{76}
$$

Expanding $\dot{y}^{n+1}$ in a Taylor series, the truncation error on the corrector becomes

$$
d\left(y^{n+1}\right) = y^{n+1} - y\left(t_{n+1}\right) = \frac{\Delta t_n^{\,3}}{12}\dddot{y}^n + O\left(\Delta t_n^{\,4}\right). \tag{77}
$$

where $d\left(y^{n+1}\right) = y^{n+1} - y\left(t_{n+1}\right)$ is the estimate of the local time truncation error of the actual solution. This expression contains the unknowns $y\left(t_{n+1}\right)$ and $\dddot{y}^n$. However, we can express (77) in terms of the known variables y_{pred}^{n+1} and y^{n+1} by substituting $\dddot{y}^n$ from (77) into (75):

$$
d\left(y^{n+1}\right) = \frac{y^{n+1} - y_{pred}^{n+1}}{3\left(1 + \frac{\Delta t_{n-1}}{\Delta t_n}\right)} + O\left(\Delta t_n^{\,4}\right). \tag{78}
$$

This result can be used to estimate the next time step Δt_{n+1} based on the requirement that a relative norm of the error for the next time step should equal a pre-set input value ε. From equa-

tion (77), we have

$$\frac{\left|d\left(y^{n+2}\right)\right|}{\left|d\left(y^{n+1}\right)\right|} = \left(\frac{\Delta t_{n+1}}{\Delta t_n}\right)^3 \frac{\left|\ddot{y}^{n+1}\right|}{\left|\ddot{y}^{n}\right|} . \tag{79}$$

Since $\ddot{y}^{n+1} = \ddot{y}^{n} + O\left(\Delta t_n\right)$, equation (79) permits the solution for Δt_{n+1}, after setting $\left|d\left(y^{n+2}\right)\right| = \varepsilon$ and neglecting higher-order terms:

$$\Delta t_{n+1} = \Delta t_n \left(\frac{\varepsilon}{\left|d\left(y^{n+1}\right)\right|}\right)^{1/3} , \tag{80}$$

which is used to compute the next time step.

In our work, we have been using the following norm proposed by Gresho *et al.*[8] for the error estimates:

$$\left|d\left(y^{n+1}\right)\right|^2 = \frac{1}{N+1} \frac{1}{\left(1+\frac{\Delta t_{n-1}}{\Delta t_n}\right)^2} \left[\frac{1}{\left(e_{\max}^{n+1}\right)^2} \sum_{i=1}^{N} \left(e_i^{n+1} - e_{i,pred}^{n+1}\right)^2 + \frac{1}{\left(R^{n+1}\right)^2} \left(R^{n+1} - R_{pred}^{n+1}\right)^2\right] \tag{81}$$

The entire algorithm for advancing the solution by one time step can be summarized as follows:

- the predictors for the nodal vector of the void ratio and the moving boundary position are computed,
- the internal nodes are relocated,
- the Jacobian matrix and the right-hand side of (61) are assembled by looping through the elements,
- the nodal vector of the void ratio is computed by solving the linear system,
- the position of the moving boundary is corrected,
- the nodal vector of the void ratio change rate and the change rate of the moving boundary position is computed for the next time step, and
- the next time step is computed.

The only user-specified parameter is ε in (80). It has been chosen equal to *0.001* in this work.

The convergence criterion on the Newton-Raphson iterative scheme for the void ratio is based on the norm of the vector of the relative error between two successive iterations and has to be less than $0.1\cdot\varepsilon$. The same convergence criterion is imposed on the moving boundary position.

Concerning the time step modification, we always accept the increase if $\Delta t_{n+1} \geq 0.8\ \Delta t_n$ but repeat the time step with $\Delta t_n = \Delta t_{n+1}$ otherwise.

3. 3 Initialization

Since $\dot{\varepsilon}^{n-1}$ and $\dot{R}^{n-1}$ are required in the equations (54) and (55), the method above cannot be applied until the third time step. The two first time steps require a special treatment.

(a) Computation of the first time step

For the first time step *n*=0, we do not use a predictor-corrector method with automatic time-step modification. The nodal values of the void ratio and the tip position are evaluated at the

time t_1 with the first-order Euler Backward scheme. Applied to $\dot{y} = f$, the scheme reads

$$y^1 = y^0 + \Delta t_0 f^1. \tag{82}$$

Applied to our problem, we have the following non-linear algebraic system of equations

$$\left[\frac{1}{\Delta t_0}\underline{\underline{M}}\left(\underline{e}^1\right) + \underline{\underline{K}}\left(\underline{e}^1\right)\right]\underline{\dot{e}}^1 = \left[\frac{1}{\Delta t_0}\underline{\underline{M}}\left(\underline{e}^1\right)\underline{e}^0 + \underline{F}\left(\underline{e}^1\right)\right], \tag{83}$$

where the integrals in $\underline{\underline{M}}$, $\underline{\underline{K}}$ and $\underline{F}$ (see (46)) are evaluated on the initial domain *[R(0)*; R_0*]*. R_0 is the artificial initial position of the expanding tip to be supplied by the user. The numerical scheme requires a small extruding bentonite in the fracture initially. In the numerical results shown in Chapter 4, 1 mm is assumed for $R_0 - R(0)$.

Newton-Raphson iterative technique is used to solve this set of equations. The algebraic system of linear equations reads

$$\begin{aligned}&\left[\frac{1}{\Delta t_0}M_{ij}\left(\underline{e}^1_{pred}\right) + K_{ij}\left(\underline{e}^1_{pred}\right) - \frac{1}{\Delta t_0}L_{ij}\left(\underline{e}^1_{pred}\right) + N_{ij}\left(\underline{e}^1_{pred}\right) - \left.\frac{\partial F_i\left(\underline{e}^1\right)_i}{\partial e^1_j}\right|_{\underline{e}^1 = \underline{e}^1_{pred}}\right]\left[e^1_j - e^1_{j,pred}\right] \\ &= \left[M_{ij}\left(\underline{e}^1_{pred}\right)\frac{1}{\Delta t_0}e^0_j + F_i\left(\underline{e}^1_{pred}\right)\right] - \left[\frac{1}{\Delta t_0}M_{ij}\left(\underline{e}^1_{pred}\right) + K_{ij}\left(\underline{e}^1_{pred}\right)\right]e^1_{j,pred}\end{aligned} \tag{84}$$

where $i = 1, 2, \ldots, N$. The first guess for the nodal values $e^1_{j,\,pred}$ will be the initial conditions except for $e^1_{N,\,pred}$, which is given by the boundary condition e_L.

The position of the moving boundary is given by the same numerical scheme (68):

$$R^1 = R^0 + \Delta t_0 C \exp\left(G\tilde{e}^1\right)\left.\frac{d\varphi_k}{dr}\right|_{r=R(t_1)} e^1_k. \tag{85}$$

Concerning the convergence on the void ratio and on the tip position, the same remarks as in the general case for n>1 apply. The time derivatives to be used in the next time step have to be evaluated. This is conveniently done by inversion of the Euler Backward scheme:

$$\dot{\underline{e}}^1 = \frac{1}{\Delta t_0}\left(\underline{e}^1 - \underline{e}^0\right), \tag{86}$$

$$\dot{R}^1 = \frac{1}{\Delta t_0}\left(R^1 - R^0\right). \tag{87}$$

As no automatic modification of the next time step is available for this scheme, the next time step will be given by

$$\Delta t_1 = \Delta t_0. \tag{88}$$

(b) Computation of the second time step

For the second time step n=1, the predictor (54) is not applicable because it requires two history vectors of acceleration. A predictor-corrector of lower order than the Adams-Bashforth/trapezoid rule scheme is used to modify automatically the time step. The steps (a) through (e) are essentially similar to those of the general case, except that the Adams-Bashforth rule is replaced by the Euler Forward rule for the predictor, the trapezoid rule by the Euler Backward rule for the corrector and the inverted trapezoid rule by the inverted Euler Backward rule for the evaluation of the time derivatives. Applied to $\dot{y} = f$, the new rules read respectively

$$y^2_{pred} = y^1 + \Delta t_1 \dot{y}^1, \tag{89}$$

$$y^2 = y^1 + \Delta t_1 f^2 \text{ and} \tag{90}$$

$$\dot{y}^2 = \frac{1}{\Delta t_1}\left(y^2 - y^1\right). \tag{91}$$

Based on the same requirements as before, the third time step can be estimated using the following equation,

$$\Delta t_2 = \Delta t_1 \left(\frac{\varepsilon}{\left| d\left(y^2\right)\right|} \right)^{1/2}, \tag{92}$$

where $$\left|d\left(y^2\right)\right|^2 = \frac{1}{N+1}\frac{1}{4}\left[\frac{1}{\left(e^2_{\max}\right)^2}\sum_{i=1}^{N}\left(e_i^2 - e^2_{i,\,pred}\right)^2 + \frac{1}{\left(R^2\right)^2}\left(R^2 - R^2_{pred}\right)^2\right]. \tag{93}$$

4 NUMERICAL EVALUATIONS

4. 1 Input data

As described in Chapter 1, experiments were done by PNC [2, 3] for expansion of bentonite through a simulated planar fracture. The initial dry density ρ_d of the bentonite specimen was measured as 1.8 g/cm^3. The dry density, ρ_d, of the bentonite is related to the void ratio as

$$e = \frac{\rho_s}{\rho_d} - 1, \tag{94}$$

where ρ_s is the density of the bentonite solid phase. ρ_s was obtained as 2.7 g/cm^3. By (94) and the initial dry density of 1.8 g/cm^3, the initial void ratio, e_o, is calculated as 0.5. The specimen was initially partially saturated with water.

The swelling pressure was measured for the dry densities of 1.5, 1.6, 1.8. and 2.0 g/cm^3. By (94), these correspond to the void ratios of 0.8, 0.6875, 0.5, and 0.35, respectively. These four points are plotted in Figure 5.

The permeability k for the specimen in saturated conditions was measured, and expressed by the following empirical relationship [3] as a function of the dry density ρ_d:

$$-\log_{10} k = 18.621 - 1.082\rho_d + \left(0.429 + 0.736 B_c\right)\rho_d^2 \text{ for } 1.0 \le \rho_d \le 1.8. \tag{95}$$

where B_c is the bentonite fraction in the sand bentonite mixture. We focus on the case where the bentonite fraction is unity. With this value, the validity range, $1.0 \le \rho_d \le 1.8$, for (95) corresponds to the void ratio range, $0.5 \le e \le 1.7$. The empirical relationship (95) is plotted as the solid line in Figure 6.

As Figure 5 and Figure 6 show, the experimental values for the swelling pressure and the permeability cover relatively low void-ratio regions. It is found later that dependencies of the swelling pressure and the permeability in greater void-ratio ranges are necessary to reproduce the experimental results by numerical simulations. The dependencies for the void ratio greater than 1.0 are assumed in the following way.

The permeability has been evaluated by (95) for the void ratio between 0.5 and 1.7 with

an increment of 0.05 as shown in Table I. By (29), a fitting line has been determined for each interval with the width of 0.05 in the void ratio. The coefficient, C_k, in (29) has been obtained for each interval by setting the values of k_0 and e_0^k equal to those at the lower bound of the interval. The fitting line for the interval between the void ratios of 1.65 and 1.7 has been extrapolated to the void ratio of 5.0. The extrapolated line is shown in Figure 6 as the dashed line connecting to the solid line.

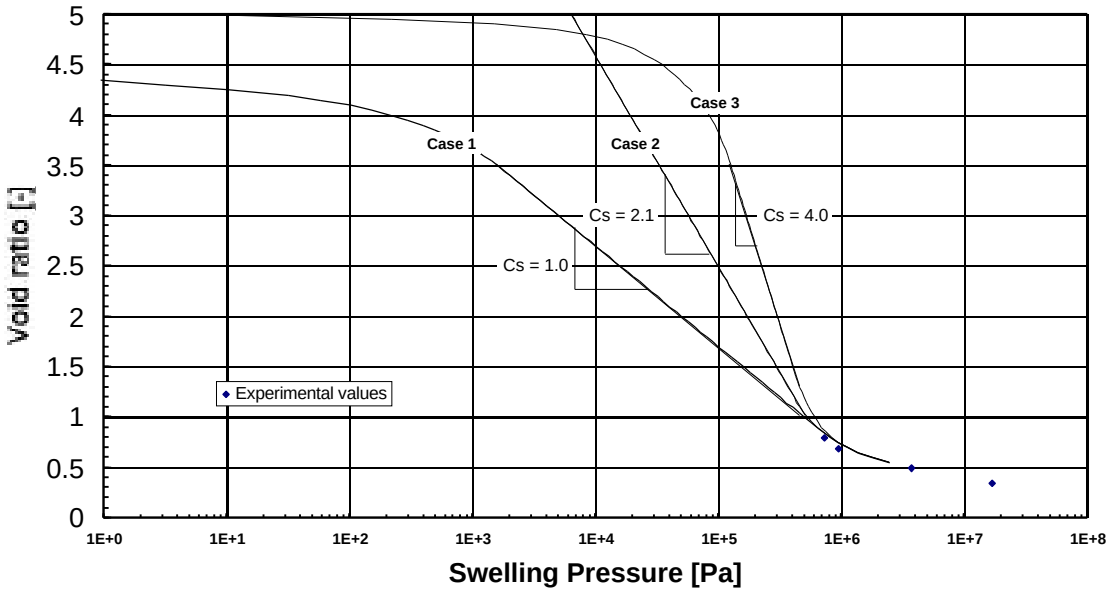

Figure 5 Relationship between the void ratio and the swelling pressure.

The swelling index, C_s, has been determined by the experimental results only for the void ratio smaller than 0.8. The swelling coefficient for the void ratio greater than 0.8 has been determined as follows. Three cases are considered. In case 1, the swelling index, C_s, at the void ratio of 0.8 is assumed to be unchanged for the void ratios between 0.8 and 3.5. Thereafter, the swelling index is assumed to decrease gradually. This is because as the void ratio increases, bentonite approaches the consistency limit, where the swelling pressure decreases rapidly. In case 2, the swelling index, C_s, for the void ratio greater than 1.0 is assumed to be 2.1. With this swelling index and the aforementioned permeability function, the function, $C\exp(Ge)$ (see eqs. (30) and (31)), becomes approximately constant for the void ratio greater than 1.5, as depicted in Figure 7. In case 3, the swelling index is assumed to be 4.0 for the void ratio between 1.0 and 3.5. The swelling index decreases thereafter as in case 1.

Once the swelling index, C_s, is assumed, the effective stress, σ', is estimated by (27). For σ'_0 and e_0^σ, the values at the lower bound of each interval are used. The swelling pressure profiles obtained by this extrapolation are plotted in Figure 5.

Thus, for each interval of the void ratio, k_0, e_0^k, C_k, σ'_0 e_0^σ, and C_s, are determined. With these values, coefficients G and C can be numerically estimated by (31). The numerical values of these coefficients are summarized in Table I.

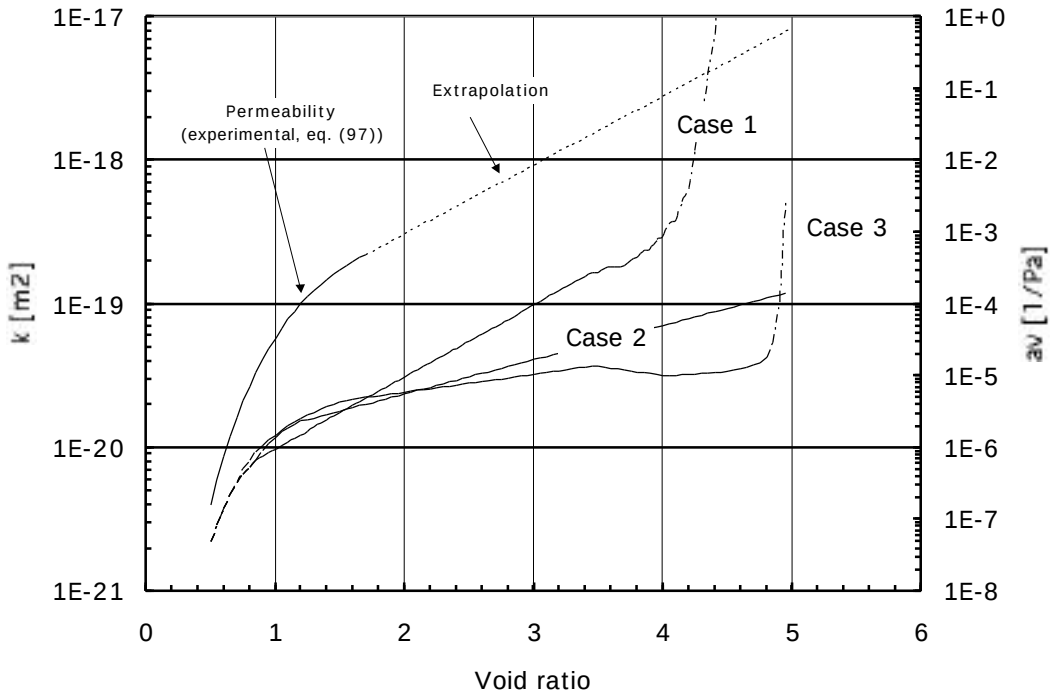

Figure 6 **The permeability (solid and dashed lines) and the compressibility coefficient (cases 1, 2, and 3) of the bentonite specimen as functions of the void ratio.**

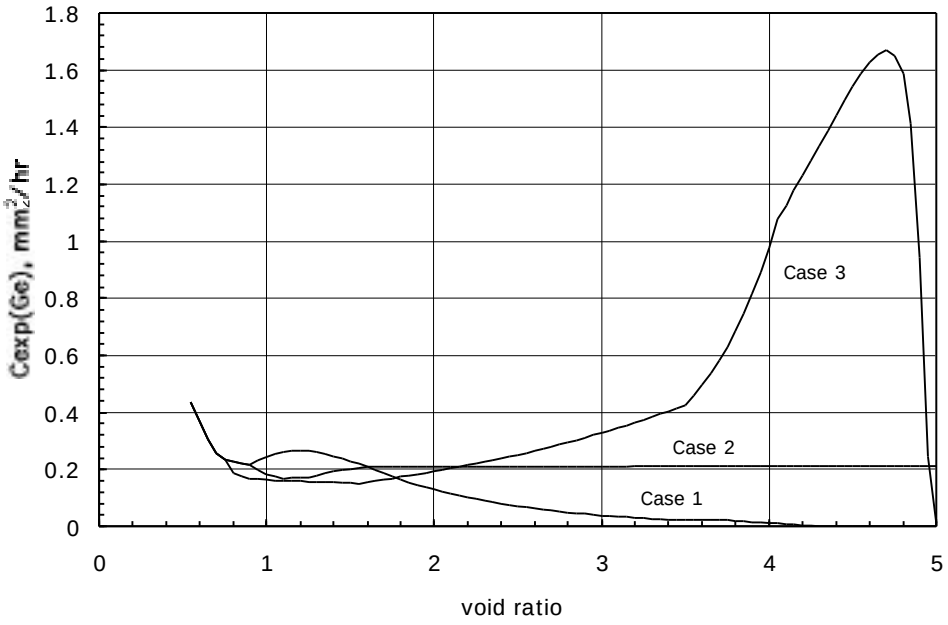

Figure 7 **Variation of Cexp(Ge) with the void ratio.**

As depicted in Figure 7, the function, $C\exp(Ge)$, decreases with the void ratio for case 1. In this case, the expansion at the tip will be slower than in the inner region. For case 2, the function is almost constant. This case will be utilized for the verification of the numerical scheme with the bench-mark analytical solution later. In case 3, the function increases as the void ratio increases for the void ratio less than 4.6. In this case, the expansion at the tip is faster than in the inner region.

4. 2 Verification with analytical solution for constant coefficients

The scheme developed in Chapter 3 is verified by comparing the numerical results obtained by the scheme with the analytical solutions. The objective of the verification is to confirm that the developed numerical scheme is properly implemented into the computer code. Even if the agreement between the numerical results obtained by the code and the analytical solution is reasonable, this verification procedure does not necessarily guarantee that the code can properly calculate for all cases. Nonetheless, this verification would provide some confidence in correctness of the code implementation. Whether or not the model represents the physical process correctly is checked later by comparing the numerical results with the experimental results. This procedure is called validation in this study. With verification and validation, we consider that the numerical calculation code developed in this study can simulate the physical processes observed in the PNC experiment properly.

Instead of the governing equation (30) we consider the following equation,

$$\beta^2 \frac{1}{r}\frac{\partial}{\partial r}\left(r\frac{\partial e}{\partial r}\right) = \frac{\partial e}{\partial t}, \quad 0 < r < a, \; t > 0, \text{ where } \beta^2 = \frac{(1+e_o)k(e_o)}{\mu a_v(e_o)}, \tag{96}$$

subject to the side conditions,

$$e(r,0) = e_o, 0 < r < a, \tag{97}$$

and

$$e(a,t) = e_L, t > 0. \tag{98}$$

e_L is the void ratio at the interface between the bentonite region and the water region, and is constant with time. The other boundary condition is implicit. The void ratio at the center, $r = 0$ must be finite. For the bentonite to expand, it is required that $e_L > e_o$. The radius of the domain, a, is assumed constant.

Equation (96) is a diffusion equation with a constant diffusion coefficient, β^2, for a finite, one-dimensional medium. The solution for the mathematical problem equivalent to (96) subject to (97) and (98) is readily available [9]. The analytical solution for early times is written as

$$e(r,t) = e_o + (e_L - e_o)\sqrt{\frac{a}{r}}\,\mathrm{erfc}\left(\frac{a-r}{2\beta\sqrt{t}}\right), \tag{99}$$

which is valid for

$$0 < \frac{\beta^2 t}{a^2} < 0.02, \text{ and } \frac{r}{a} \approx 1, r < a. \tag{100}$$

In early times, the expansion occurs only in the vicinity of the tip at $r = a$. For the water that has just entered the bentonite region at the $r = a$, the bentonite is as if it were a semi-infinite medium. The analytical solution is, therefore, written in terms of the complementary error function, which appears for the diffusion process in a semi-infinite medium.

The water flow rate at the boundary, $r = a$, into the bentonite is estimated by the Darcy's

law as

$$q\big|_{r=a} = \frac{k(e_L)}{\mu a_v(e_L)} \frac{\partial e}{\partial r}\bigg|_{r=a}. \tag{101}$$

With (99), the water flow rate is obtained as

$$q\big|_{r=a} = \frac{k(e_L)}{\mu a_v(e_L)} (e_L - e_o) \left(-\frac{1}{2a} + \frac{1}{\beta\sqrt{\pi t}} \right), \tag{102}$$

which is also valid for the conditions given by (100).

The total water volume, Q_T, that has entered the bentonite region through the boundary at $r = a$ by time t is obtained by integrating (102) with respect to time and multiplying the resultant expression by the cross-sectional area of the boundary, as

$$Q_T = 2\pi a L \frac{k(e_L)}{\mu a_v(e_L)} (e_L - e_o) \left(-\frac{t}{2a} + \frac{2\sqrt{t}}{\beta\sqrt{\pi}} \right), \tag{103}$$

where L is the aperture of the fracture.

Suppose that, due to this amount of water, the radius of the bentonite domain is increased by Δa. Then, the total volume (bentonite solid phase plus water) in this increment is calculated as $\pi L\left\{(a + \Delta a)^2 - a^2\right\} = \pi L \Delta a (2a + \Delta a)$. If we assume that the void ratio of this increment is equal to e_L, then we have

$$e_L = \frac{Q_T}{\pi L \Delta a (2a + \Delta a) \ - Q_T} \tag{104}$$

Thus, the boundary movement Δa is estimated by

$$\Delta a = -a + \sqrt{a^2 + 2a\left(1 + \frac{1}{e_L}\frac{k(e_L)}{\mu a_v(e_L)}(e_L - e_o)\left(-\frac{t}{2a} + \frac{2\sqrt{t}}{\beta\sqrt{\pi}}\right)\right)}, \quad 0 < \frac{\beta^2 t}{a^2} < 0.02. \tag{105}$$

From Table I, the value of $\dfrac{k(e_o)}{\mu a_v(e_o)}$ is obtained as 0.437 mm^2/hr (see the values of $C\exp(Ge)$ for the void ratio of 0.5 for each case). Then, the value of β^2 is calculated as 0.437•(1 + 0.5) = 0.654 mm^2/hr. The value of β is 0.809 mm/hr$^{1/2}$. The initial radius of the bentonite specimen in the PNC experiment was 25 mm. Thus, the upper bound of the time given by (100) is calculated as $0.02 \bullet 25^2$ [mm^2] / 0.654 [mm^2/hr] = 19 [hr]. With these values, it is found that, of the two terms in the bracket of the right hand side of (105), the last term, $\dfrac{2\sqrt{t}}{\beta\sqrt{\pi}}$, is dominant to the other term, $t/2a$. For a small expansion, $(\Delta a)^2$ is negligibly small. In the denominator of (104), that term can be dropped. Then, (105) is further approximated as

$$\Delta a \approx \left(1 + \frac{1}{e_L}\frac{k(e_L)}{\mu a_v(e_L)}(e_L - e_o)\right)\frac{2}{\beta\sqrt{\pi}}\sqrt{t}\,. \tag{106}$$

(106) indicates that the bentonite expansion is proportional to the square root of time. This is the same behavior as observed in the experiment by PNC [2, 3].

Table I Determination of the permeability, the compressibility coefficient, coefficients C, and G.

Void ratio	k [m^2]	Ck	Case 1					Case 2					Case 3				
			Cs	σ_o' [Pa]	C [m^2/sec]	G	Cexp(Ge) [mm^2/hr]	Cs	σ_o' [Pa]	C [m^2/sec]	G	Cexp(Ge) [mm^2/hr]	Cs	σ_o' [Pa]	C [m^2/sec]	G	Cexp(Ge) [mm^2/hr]
0.5	4.00E-21			3.71E+06					3.71E+06					3.71E+06			
0.55	6.01E-21	0.283	0.28	2.46E+06	1.27E-10	-0.08	0.437	0.28	2.46E+06	1.27E-10	-0.08	0.437	0.28	2.46E+06	1.27E-10	-0.08	0.437
0.6	8.65E-21	0.315	0.34	1.75E+06	7.46E-11	0.53	0.369	0.34	1.75E+06	7.46E-11	0.53	0.369	0.34	1.75E+06	7.46E-11	0.53	0.369
0.65	1.20E-20	0.350	0.44	1.35E+06	3.55E-11	1.34	0.305	0.44	1.35E+06	3.55E-11	1.34	0.305	0.44	1.35E+06	3.55E-11	1.34	0.305
0.7	1.62E-20	0.388	0.57	1.10E+06	1.92E-11	1.89	0.259	0.57	1.10E+06	1.92E-11	1.89	0.259	0.57	1.10E+06	1.92E-11	1.89	0.259
0.75	2.11E-20	0.429	0.70	9.35E+05	1.37E-11	2.07	0.234	0.70	9.35E+05	1.37E-11	2.07	0.234	0.70	9.35E+05	1.37E-11	2.07	0.234
0.8	2.69E-20	0.474	0.80	8.10E+05	1.28E-11	1.98	0.226	0.80	8.10E+05	1.28E-11	1.98	0.226	1.00	8.34E+05	6.67E-12	2.56	0.186
0.85	3.36E-20	0.521	0.90	7.13E+05	1.26E-11	1.86	0.220	0.90	7.13E+05	1.26E-11	1.86	0.220	1.20	7.57E+05	5.84E-12	2.50	0.176
0.9	4.11E-20	0.573	1.00	6.35E+05	1.28E-11	1.72	0.216	1.00	6.35E+05	1.28E-11	1.72	0.216	1.40	6.98E+05	5.55E-12	2.38	0.170
0.95	4.94E-20	0.628	1.00	5.66E+05	1.76E-11	1.37	0.231	1.20	5.77E+05	1.04E-11	1.75	0.197	1.60	6.49E+05	5.54E-12	2.23	0.166
1	5.84E-20	0.687	1.00	5.05E+05	2.37E-11	1.05	0.244	1.40	5.32E+05	9.23E-12	1.71	0.184	1.80	6.09E+05	5.71E-12	2.07	0.164
1.05	6.81E-20	0.750	1.00	4.50E+05	3.14E-11	0.77	0.253	1.60	4.95E+05	8.73E-12	1.63	0.174	2.00	5.75E+05	6.00E-12	1.92	0.162
1.1	7.84E-20	0.818	1.00	4.01E+05	4.10E-11	0.51	0.260	1.80	4.64E+05	8.57E-12	1.54	0.167	2.20	5.46E+05	6.38E-12	1.77	0.161
1.15	8.92E-20	0.890	1.00	3.57E+05	5.28E-11	0.28	0.264	1.90	4.37E+05	9.70E-12	1.38	0.170	2.40	5.20E+05	6.84E-12	1.63	0.160
1.2	1.00E-19	0.967	1.00	3.18E+05	6.70E-11	0.08	0.265	2.00	4.12E+05	1.09E-11	1.23	0.171	2.60	4.97E+05	7.36E-12	1.49	0.159
1.25	1.12E-19	1.050	1.00	2.84E+05	8.39E-11	-0.11	0.263	2.10	3.90E+05	1.22E-11	1.10	0.173	2.80	4.77E+05	7.93E-12	1.37	0.158
1.3	1.24E-19	1.138	1.00	2.53E+05	1.04E-10	-0.28	0.260	2.10	3.69E+05	1.51E-11	0.93	0.181	3.00	4.59E+05	8.55E-12	1.26	0.157
1.35	1.36E-19	1.233	1.00	2.25E+05	1.27E-10	-0.43	0.254	2.10	3.50E+05	1.84E-11	0.77	0.188	3.20	4.43E+05	9.20E-12	1.15	0.156
1.4	1.48E-19	1.333	1.00	2.01E+05	1.53E-10	-0.58	0.247	2.10	3.31E+05	2.23E-11	0.63	0.194	3.40	4.28E+05	9.89E-12	1.05	0.155
1.45	1.61E-19	1.440	1.00	1.79E+05	1.84E-10	-0.70	0.238	2.10	3.13E+05	2.66E-11	0.50	0.199	3.60	4.15E+05	1.06E-11	0.96	0.153
1.5	1.73E-19	1.554	1.00	1.60E+05	2.18E-10	-0.82	0.229	2.10	2.97E+05	3.16E-11	0.39	0.203	3.80	4.03E+05	1.13E-11	0.88	0.152
1.55	1.85E-19	1.675	1.00	1.42E+05	2.56E-10	-0.93	0.218	2.10	2.81E+05	3.71E-11	0.28	0.205	4.00	3.91E+05	1.21E-11	0.80	0.150
1.6	1.98E-19	1.804	1.00	1.27E+05	2.98E-10	-1.03	0.208	2.10	2.66E+05	4.32E-11	0.18	0.207	4.00	3.80E+05	1.41E-11	0.70	0.156
1.65	2.10E-19	1.941	1.00	1.13E+05	3.44E-10	-1.12	0.196	2.10	2.52E+05	4.99E-11	0.09	0.208	4.00	3.69E+05	1.63E-11	0.61	0.160
1.7	2.22E-19	2.087	1.00	1.01E+05	3.94E-10	-1.20	0.185	2.10	2.38E+05	5.72E-11	0.01	0.208	4.00	3.59E+05	1.86E-11	0.53	0.165
1.75	2.34E-19	2.087	1.00	8.97E+04	3.94E-10	-1.20	0.174	2.10	2.26E+05	5.72E-11	0.01	0.208	4.00	3.49E+05	1.86E-11	0.53	0.169
1.8	2.48E-19	2.087	1.00	8.00E+04	3.94E-10	-1.20	0.164	2.10	2.14E+05	5.72E-11	0.01	0.208	4.00	3.39E+05	1.86E-11	0.53	0.174
1.85	2.62E-19	2.087	1.00	7.13E+04	3.94E-10	-1.20	0.154	2.10	2.02E+05	5.72E-11	0.01	0.209	4.00	3.29E+05	1.86E-11	0.53	0.178
1.9	2.76E-19	2.087	1.00	6.35E+04	3.94E-10	-1.20	0.145	2.10	1.91E+05	5.72E-11	0.01	0.209	4.00	3.20E+05	1.86E-11	0.53	0.183
1.95	2.92E-19	2.087	1.00	5.66E+04	3.94E-10	-1.20	0.137	2.10	1.81E+05	5.72E-11	0.01	0.209	4.00	3.11E+05	1.86E-11	0.53	0.188
2	3.09E-19	2.087	1.00	5.05E+04	3.94E-10	-1.20	0.129	2.10	1.71E+05	5.72E-11	0.01	0.209	4.00	3.02E+05	1.86E-11	0.53	0.193
2.05	3.26E-19	2.087	1.00	4.50E+04	3.94E-10	-1.20	0.121	2.10	1.62E+05	5.72E-11	0.01	0.209	4.00	2.93E+05	1.86E-11	0.53	0.198
2.1	3.45E-19	2.087	1.00	4.01E+04	3.94E-10	-1.20	0.114	2.10	1.54E+05	5.72E-11	0.01	0.209	4.00	2.85E+05	1.86E-11	0.53	0.203
2.15	3.64E-19	2.087	1.00	3.57E+04	3.94E-10	-1.20	0.108	2.10	1.45E+05	5.72E-11	0.01	0.209	4.00	2.77E+05	1.86E-11	0.53	0.209
2.2	3.85E-19	2.087	1.00	3.18E+04	3.94E-10	-1.20	0.101	2.10	1.38E+05	5.72E-11	0.01	0.209	4.00	2.69E+05	1.86E-11	0.53	0.214
2.25	4.07E-19	2.087	1.00	2.84E+04	3.94E-10	-1.20	0.096	2.10	1.30E+05	5.72E-11	0.01	0.209	4.00	2.61E+05	1.87E-11	0.53	0.220
2.3	4.30E-19	2.087	1.00	2.53E+04	3.94E-10	-1.20	0.090	2.10	1.23E+05	5.72E-11	0.01	0.209	4.00	2.54E+05	1.87E-11	0.53	0.226
2.35	4.54E-19	2.087	1.00	2.25E+04	3.94E-10	-1.20	0.085	2.10	1.17E+05	5.72E-11	0.01	0.209	4.00	2.47E+05	1.87E-11	0.53	0.232

Void ratio	k [m^2]	Ck	Case 1					Case 2					Case 3				
			Cs	σ_o' [Pa]	C [m^2/sec]	G	Cexp(Ge) [mm^2/hr]	Cs	σ_o' [Pa]	C [m^2/sec]	G	Cexp(Ge) [mm^2/hr]	Cs	σ_o' [Pa]	C [m^2/sec]	G	Cexp(Ge) [mm^2/hr]
2.4	4.80E-19	2.087	1.00	2.01E+04	3.94E-10	-1.20	0.080	2.10	1.11E+05	5.72E-11	0.01	0.209	4.00	2.40E+05	1.87E-11	0.53	0.238
2.45	5.07E-19	2.087	1.00	1.79E+04	3.94E-10	-1.20	0.075	2.10	1.05E+05	5.72E-11	0.01	0.209	4.00	2.33E+05	1.87E-11	0.53	0.245
2.5	5.36E-19	2.087	1.00	1.60E+04	3.94E-10	-1.20	0.071	2.10	9.91E+04	5.72E-11	0.01	0.210	4.00	2.26E+05	1.87E-11	0.53	0.251
2.55	5.66E-19	2.087	1.00	1.42E+04	3.94E-10	-1.20	0.067	2.10	9.38E+04	5.72E-11	0.01	0.210	4.00	2.20E+05	1.87E-11	0.53	0.258
2.6	5.99E-19	2.087	1.00	1.27E+04	3.94E-10	-1.20	0.063	2.10	8.88E+04	5.72E-11	0.01	0.210	4.00	2.14E+05	1.87E-11	0.53	0.265
2.65	6.33E-19	2.087	1.00	1.13E+04	3.94E-10	-1.20	0.059	2.10	8.41E+04	5.72E-11	0.01	0.210	4.00	2.08E+05	1.87E-11	0.53	0.272
2.7	6.68E-19	2.087	1.00	1.01E+04	3.94E-10	-1.20	0.056	2.10	7.96E+04	5.72E-11	0.01	0.210	4.00	2.02E+05	1.87E-11	0.53	0.279
2.75	7.06E-19	2.087	1.00	8.97E+03	3.94E-10	-1.20	0.052	2.10	7.54E+04	5.72E-11	0.01	0.210	4.00	1.96E+05	1.87E-11	0.53	0.287
2.8	7.47E-19	2.087	1.00	8.00E+03	3.94E-10	-1.20	0.049	2.10	7.13E+04	5.72E-11	0.01	0.210	4.00	1.90E+05	1.87E-11	0.53	0.294
2.85	7.89E-19	2.087	1.00	7.13E+03	3.94E-10	-1.20	0.047	2.10	6.75E+04	5.72E-11	0.01	0.210	4.00	1.85E+05	1.87E-11	0.53	0.302
2.9	8.34E-19	2.087	1.00	6.35E+03	3.94E-10	-1.20	0.044	2.10	6.39E+04	5.72E-11	0.01	0.210	4.00	1.80E+05	1.87E-11	0.53	0.310
2.95	8.81E-19	2.087	1.00	5.66E+03	3.94E-10	-1.20	0.041	2.10	6.05E+04	5.72E-11	0.01	0.210	4.00	1.75E+05	1.87E-11	0.53	0.319
3	9.31E-19	2.087	1.00	5.05E+03	3.94E-10	-1.20	0.039	2.10	5.73E+04	5.72E-11	0.01	0.210	4.00	1.70E+05	1.87E-11	0.53	0.327
3.05	9.84E-19	2.087	1.00	4.50E+03	3.94E-10	-1.20	0.037	2.10	5.42E+04	5.72E-11	0.01	0.210	4.00	1.65E+05	1.87E-11	0.53	0.336
3.1	1.04E-18	2.087	1.00	4.01E+03	3.94E-10	-1.20	0.034	2.10	5.13E+04	5.72E-11	0.01	0.210	4.00	1.60E+05	1.87E-11	0.53	0.345
3.15	1.10E-18	2.087	1.00	3.57E+03	3.94E-10	-1.20	0.032	2.10	4.86E+04	5.72E-11	0.01	0.211	4.00	1.56E+05	1.87E-11	0.53	0.354
3.2	1.16E-18	2.087	1.00	3.18E+03	3.94E-10	-1.20	0.031	2.10	4.60E+04	5.72E-11	0.01	0.211	4.00	1.51E+05	1.87E-11	0.53	0.364
3.25	1.23E-18	2.087	1.00	2.84E+03	3.94E-10	-1.20	0.029	2.10	4.36E+04	5.72E-11	0.01	0.211	4.00	1.47E+05	1.87E-11	0.53	0.373
3.3	1.30E-18	2.087	1.00	2.53E+03	3.94E-10	-1.20	0.027	2.10	4.12E+04	5.72E-11	0.01	0.211	4.00	1.43E+05	1.87E-11	0.53	0.383
3.35	1.37E-18	2.087	1.00	2.25E+03	3.94E-10	-1.20	0.026	2.10	3.90E+04	5.72E-11	0.01	0.211	4.00	1.39E+05	1.87E-11	0.53	0.394
3.4	1.45E-18	2.087	1.00	2.01E+03	3.94E-10	-1.20	0.024	2.10	3.69E+04	5.72E-11	0.01	0.211	4.00	1.35E+05	1.87E-11	0.53	0.404
3.45	1.53E-18	2.087	1.00	1.79E+03	3.94E-10	-1.20	0.023	2.10	3.50E+04	5.72E-11	0.01	0.211	4.00	1.31E+05	1.87E-11	0.53	0.415
3.5	1.62E-18	2.087	1.00	1.60E+03	3.94E-10	-1.20	0.021	2.10	3.31E+04	5.72E-11	0.01	0.211	4.00	1.27E+05	1.87E-11	0.53	0.426
3.55	1.71E-18	2.087	0.90	1.40E+03	1.07E-09	-1.45	0.022	2.10	3.13E+04	5.72E-11	0.01	0.211	3.80	1.24E+05	2.18E-11	0.50	0.460
3.6	1.81E-18	2.087	0.90	1.24E+03	1.07E-09	-1.45	0.021	2.10	2.97E+04	5.72E-11	0.01	0.211	3.60	1.20E+05	2.60E-11	0.46	0.497
3.65	1.91E-18	2.087	0.80	1.07E+03	3.82E-09	-1.77	0.021	2.10	2.81E+04	5.72E-11	0.01	0.211	3.40	1.16E+05	3.15E-11	0.43	0.537
3.7	2.02E-18	2.087	0.70	9.08E+02	1.96E-08	-2.19	0.022	2.10	2.66E+04	5.72E-11	0.01	0.211	3.20	1.12E+05	3.90E-11	0.38	0.582
3.75	2.13E-18	2.087	0.60	7.49E+02	1.74E-07	-2.73	0.022	2.10	2.52E+04	5.72E-11	0.01	0.211	3.00	1.07E+05	4.97E-11	0.34	0.631
3.8	2.25E-18	2.087	0.60	6.18E+02	1.74E-07	-2.73	0.019	2.10	2.38E+04	5.72E-11	0.01	0.211	2.80	1.03E+05	6.55E-11	0.28	0.686
3.85	2.38E-18	2.087	0.50	4.91E+02	3.85E-06	-3.50	0.019	2.10	2.26E+04	5.72E-11	0.01	0.212	2.60	9.86E+04	8.96E-11	0.22	0.747
3.9	2.51E-18	2.087	0.50	3.90E+02	3.85E-06	-3.50	0.016	2.10	2.14E+04	5.72E-11	0.01	0.212	2.40	9.39E+04	1.29E-10	0.14	0.815
3.95	2.66E-18	2.087	0.40	2.93E+02	4.29E-04	-4.65	0.016	2.10	2.02E+04	5.72E-11	0.01	0.212	2.20	8.92E+04	1.98E-10	0.06	0.891
4	2.81E-18	2.087	0.40	2.19E+02	4.29E-04	-4.65	0.013	2.10	1.91E+04	5.72E-11	0.01	0.212	2.00	8.42E+04	3.29E-10	-0.05	0.978
4.05	2.97E-18	2.087	0.30	1.49E+02	1.23E+00	-6.57	0.012	2.10	1.81E+04	5.72E-11	0.01	0.212	1.80	7.90E+04	6.10E-10	-0.18	1.077
4.1	3.13E-18	2.087	0.30	1.02E+02	1.23E+00	-6.57	0.009	2.10	1.71E+04	5.72E-11	0.01	0.212	1.70	7.38E+04	8.76E-10	-0.25	1.127
4.15	3.31E-18	2.087	0.20	5.73E+01	1.26E+07	-10.41	0.008	2.10	1.62E+04	5.72E-11	0.01	0.212	1.60	6.87E+04	1.32E-09	-0.34	1.177
4.2	3.50E-18	2.087	0.20	3.22E+01	1.26E+07	-10.41	0.005	2.10	1.54E+04	5.72E-11	0.01	0.212	1.50	6.36E+04	2.09E-09	-0.43	1.229
4.25	3.70E-18	2.087	0.10	1.02E+01	2.52E+28	-21.92	0.003	2.10	1.45E+04	5.72E-11	0.01	0.212	1.40	5.86E+04	3.55E-09	-0.54	1.281
4.3	3.91E-18	2.087	0.10	3.22E+00	2.52E+28	-21.92	0.001	2.10	1.38E+04	5.72E-11	0.01	0.212	1.30	5.36E+04	6.55E-09	-0.67	1.335
4.35	4.13E-18	2.087	0.09	8.96E-01	1.68E+33	-24.48	0.000	2.10	1.30E+04	5.72E-11	0.01	0.212	1.20	4.87E+04	1.34E-08	-0.82	1.388
4.4	4.36E-18	2.087	0.09	2.49E-01	1.68E+33	-24.48	0.000	2.10	1.23E+04	5.72E-11	0.01	0.212	1.10	4.39E+04	3.12E-08	-0.99	1.441
4.45	4.61E-18	2.087	0.08	5.91E-02	2.44E+39	-27.68	0.000	2.10	1.17E+04	5.72E-11	0.01	0.212	1.00	3.91E+04	8.61E-08	-1.20	1.493

Void ratio	k [m^2]	Ck	Case 1					Case 2					Case 3				
			Cs	σ_o' [Pa]	C [m^2/sec]	G	Cexp(Ge) [mm^2/hr]	Cs	σ_o' [Pa]	C [m^2/sec]	G	Cexp(Ge) [mm^2/hr]	Cs	σ_o' [Pa]	C [m^2/sec]	G	Cexp(Ge) [mm^2/hr]
4.5	4.87E-18	2.087	0.08	1.40E-02	2.44E+39	-27.68	0.000	2.10	1.11E+04	5.72E-11	0.01	0.213	0.90	3.44E+04	2.99E-07	-1.45	1.543
4.55	5.15E-18	2.087	0.07	2.71E-03	3.02E+47	-31.79	0.000	2.10	1.05E+04	5.72E-11	0.01	0.213	0.80	2.98E+04	1.42E-06	-1.77	1.588
4.6	5.44E-18	2.087	0.07	5.23E-04	3.02E+47	-31.79	0.000	2.10	9.91E+03	5.72E-11	0.01	0.213	0.70	2.53E+04	1.05E-05	-2.19	1.627
4.65	5.75E-18	2.087	0.06	7.67E-05	3.16E+58	-37.27	0.000	2.10	9.38E+03	5.72E-11	0.01	0.213	0.60	2.09E+04	1.53E-04	-2.73	1.656
4.7	6.08E-18	2.087	0.06	1.13E-05	3.16E+58	-37.27	0.000	2.10	8.88E+03	5.72E-11	0.01	0.213	0.50	1.66E+04	6.51E-03	-3.50	1.668
4.75	6.42E-18	2.087	0.05	1.13E-06	1.76E+74	-44.95	0.000	2.10	8.41E+03	5.72E-11	0.01	0.213	0.40	1.24E+04	1.82E+00	-4.65	1.652
4.8	6.79E-18	2.087	0.05	1.13E-07	1.76E+74	-44.95	0.000	2.10	7.96E+03	5.72E-11	0.01	0.213	0.30	8.46E+03	2.21E+04	-6.57	1.586
4.85	7.17E-18	2.087	0.04	6.33E-09	2.20E+98	-56.46	0.000	2.10	7.54E+03	5.72E-11	0.01	0.213	0.20	4.76E+03	3.31E+12	-10.41	1.414
4.9	7.58E-18	2.087	0.04	3.56E-10	2.20E+98	-56.46	0.000	2.10	7.13E+03	5.72E-11	0.01	0.213	0.10	1.51E+03	1.18E+37	-21.92	0.945
4.95	8.01E-18	2.087	0.03	7.67E-12	2.00E+139	-75.65	0.000	2.10	6.75E+03	5.72E-11	0.01	0.213	0.06	2.21E+02	9.10E+69	-37.27	0.244
5	8.46E-18	2.087	0.03	1.65E-13	2.00E+139	-75.65	0.000	2.10	6.39E+03	5.72E-11	0.01	0.213	0.03	4.76E+00	5.76E+152	-75.65	0.011

In Figure 8, two dashed curves are plotted by (105) for two values of e_L: 2.0 and 4.0. Also plotted are numerical results for case 2, where the values of $C\exp(Ge)$ are constant at 0.21 mm^2/hr for the void ratio greater than 1.5 (see the column for $C\exp(Ge)$ for case 2 in Table I). For the curves by the analytical solution (105), the value, 0.21 mm^2/hr, is used also for $\frac{k(e_L)}{\mu a_v(e_L)}$.

For numerical simulations, as has been discussed in page 19, a small extruding bentonite in the fracture is required initially. 1 mm is assumed for all the calculations hereafter. For the numerical results shown in Figure 8 to Figure 10, *R(0)* and R_0 are set 24 mm and 25 mm, respectively.

The agreement between the analytical and the numerical for the case of e_L = 2.0 is remarkable. The agreement is worse for e_L = 4.0. This is because the estimate of the water flow rate by (101) evaluated at the fixed point $r = a$ is not good for a larger expansion. For a greater void ratio, e_L, at the interface, the expansion is faster because with a greater e_L, the gradient of e at the interface is greater, resulting in a greater water flux into the bentonite region.

With these comparisons, it can be said that the numerical scheme has been correctly implemented into the computer code.

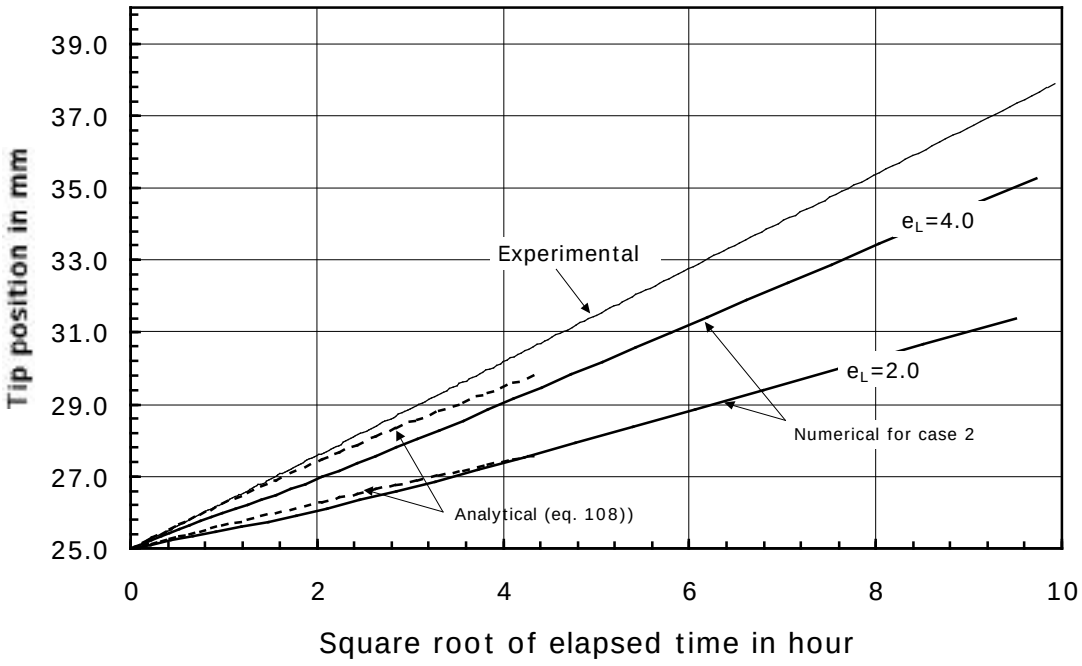

Figure 8 Comparison of numerical results of case 2 with the analytical solution (105).

The PNC experiment gives 1.3 mm/hr$^{1/2}$ for the proportionality factor. The numerical results show slower expansion than the experimental results. However, the analytical solution for e_L = 4.0 shows a good agreement for the time smaller than 1 hour. This implies that in very early times the driving force for the expansion set by the void ratio difference, $e_L - e_o$ = 4.0 - 0.5 = 3.5, at the expanding tip would be similar to that actually realized in the experiment. In very early times, the expansion is so small that difference in the bentonite properties $\frac{k(e)}{\mu a_v(e)}$ inside the ex-

panding bentonite has negligible effects on the expansion speed. The curve obtained by the analytical solution deviates from the experimental curve because for the analytical solution the bentonite properties $\frac{k(e)}{\mu a_v(e)}$ are assumed to be equal to that at the void ratio of 0.5 everywhere except at the tip (see eq. (96)). Thus, it is considered that the void ratio at the tip, e_L = 4.0, is an appropriate estimate, but the properties of the expanding bentonite must be adjusted to obtain a better agreement with the experimental results.

4. 3 Validation with experimental results

Having confirmed that the numerical scheme is properly implemented in the computer code, SABRE, we consider in this section whether the model developed in Chapter 2 represents the physical mechanisms of the bentonite swelling correctly. For this objective, the numerical results obtained by the computer code are compared with the experimental results. Because some key parameters such as the void ratio at the tip, the swelling pressure and the permeability of the expanding bentonite for the void ratio greater than 1.0 were not measured in the experiment, we estimate those parameters by parametric surveys. In this regard, the validation attempted here is not a complete one.

Figure 9 shows five curves obtained by the SABRE code and the experimental result. Of the five curves for the numerical results, two curves are for case 1 with e_L = 2.0 and 4.0, two curves for case 2 with e_L = 2.0 and 4.0, and one curve for case 3 with e_L = 4.05. From Figure 7, case 1 represents the case where the function, $C\exp(Ge)$, which determines the speed of expansion, decreases the void ratio increases. Thus, the expansion of the bentonite is slower in the vicinity of the tip than in the inner region. As has been observed in the previous section, an almost constant function is assumed for $C\exp(Ge)$ in case 2. Case 3 represents the case with an increasing $C\exp(Ge)$ as a function of the void ratio.

It is observed that in case 1 or case 2 the expansion is not fast enough to reproduce the experimental results for the void ratio, e_L, at the tip equal to 2.0 or 4.0. It has been confirmed by additional numerical simulations that even though a value greater than 4.0 is assumed for e_L, the numerical simulations cannot give a similar expansion as the experimental results. If we consider that the bentonite has the consistency limit for it to be regarded as one solid phase rather than a suspension phase of colloid particles in water, too large a void ratio at the tip is not physically permissible. Thus, it is considered that the properties represented by the functional forms assumed for cases 1 and 2 do not represent the properties of the bentonite specimen used in the experiment.

The curve for case 3, on the other hand, shows a good agreement with the experimental result. The void ratio of 4.05 at the tip also coincides with the value 4.0, with which the analytical solution could show a very good agreement with the experimental result for very early times (see Figure 8). The numerical solution for case 3 gives a good agreement also for later times.

Figure 10 shows the spatial distributions of the void ratio in the bentonite expanding in the planar fracture. Profiles are drawn for 1, 10, and 90 hours for case 3. The void ratio at the fracture intersection with the bulk bentonite is maintained at 0.5. The profiles show that the gradient of the void ratio is at the tip smaller than at the fracture intersection. The gradient at the tip decreases as time proceeds.

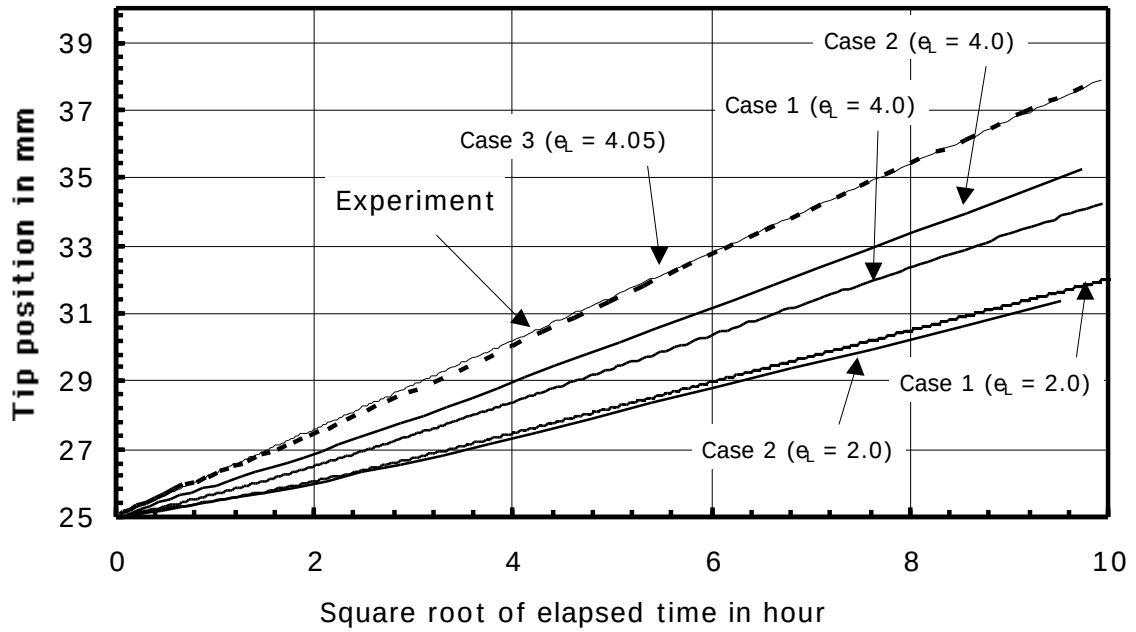

Figure 9 **Comparison of numerical results for cases 1, 2, and 3 for different void ratios at the tip with the experimental results.**

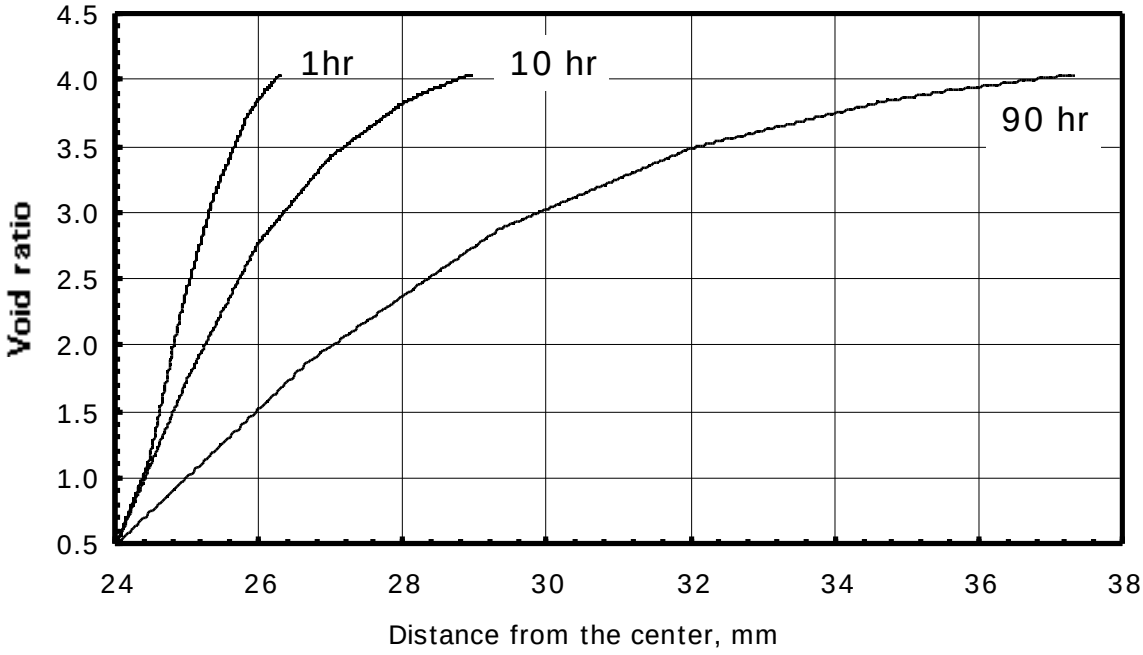

Figure 10 **Spatial distributions of the void ratio in the expanding bentonite in the fracture for different times for case 3.**

5 SUMMARY OF ASSUMPTIONS AND LIMITATIONS OF THE MODEL

(a) Application of one-dimensional consolidation theory

Limitations of the present model involve the method of handling bentonite deformation [4]. The one-dimensional consolidation theory is a simple concept that has been found to be of practical value under many field conditions. However, there may be situations where one will have to consider the complex relation between changes in pore pressure and the general effective stress tensor. For example, in the PNC experiment, it was shown that the expansion is faster for a larger aperture of the fracture [2, 3]. The effect of the friction force at the interface between the fracture surface and the expanding bentonite is considered more prominent for a smaller fracture aperture. It was pointed out [2, 3] that with an aperture greater than 1 mm the effect of the aperture on the expansion speed is less apparent. Thus, the numerical results obtained by the present model can be considered to represent the expansion with a sufficiently large aperture where the friction force effect is negligible.

To reproduce the aperture dependency of the bentonite expansion in a fracture, we must consider the relation between pore water pressure and the effective stress tensor. In such a situation, we do not know a priori the quantity de/dp_w in (8) until we have solved an independent equation relating changes in effective stress to the consequent strains. For a rigorous solution for the problem, we need two equations: one for fluid flow as given by (1) and another for force equilibrium relating changes in effective stress to the deformation (strain) of the bentonite skeleton. To couple the two equations properly, one would not only need to know the manner in which changes in the head affect the stress tensor but also the three-dimensional stress-strain relationship. The problem is further complicated by the fact that in a water-saturated bentonite, the deformation is not only governed by changes in stress induced by changes in pore pressure but also by the seepage stresses and the drag forces imposed on individual grains by moving water. The one-dimensional consolidation theory used in this model does not take these complex factors into account.

(b) The bentonite is saturated with water (Eq. (21)).

The experiment was performed with partially saturated samples [2, 3]. Thus, this assumption differs from the experimental condition. Nevertheless, the numerical simulations show a good agreement (Figure 9). In the model, the void ratios at the tip and the fracture intersection are assumed constant (see below also). Therefore, the agreement between the experimental and numerical implies that the *extruding* bentonite in the experiment was actually saturated with water. It is considered that water supplied from the fracture wets the bentonite in the vicinity of the fracture intersection, and that when the bentonite extruded out into the fracture, the bentonite was already saturated with water.

(c) Void ratio at the expanding tip is constant (Eq. (33)).

This is an assumption that has not been tested by experiments. However, from the numerical simulation, it has been found that the void ratio at the tip has a very strong influence on the expansion speed. For example, as shown in Figure 9, the expansion speed, which is approximately represented by the slope of the curves, is greater for the greater void ratio at the tip. If the void ratio at the tip were not constant with time, the expansion would not be expressed in a straight line in the tip location versus square root of time diagram. Thus, the constant void ratio at the tip seems a valid assumption, although the final validation of this assumption is made only by experimental measurements.

The assumed boundary condition allows indefinite expansion of bentonite. The bentonite expansion terminates when the bentonite supply at the inner boundary or the water supply at the tip does. The water supply is dependent on the fracture network geometry, which determines the water flow around the EBS. The bentonite expansion would in return affect the water flow around the EBS.

(d) Void ratio at the fracture intersection is constant (Eq. (34)).

(e) The same volume of bentonite with the void ratio e_o as the water volume entering the bulk bentonite extrudes into the fracture (Figure 4).

These assumption together with assumption (d) have been made for simplicity of the model, and not tested experimentally. As shown in eq. (40), the expansion is determined only by the amount of water taken at the tip. The fact that the analytical solution representing practically a semi-infinite medium shows a good agreement with the experimental expansion means the same thing. We need to confirm experimentally also the validity of these assumptions.

(f) Void-ratio dependencies for permeability and compressibility coefficient

As discussed in section 4.3, from the model simulations, it is considered that the dependency should be like the one assumed for case 3. This, however, should be checked by the experiment.

Thus, to finally validate the assumptions and the model, experimental studies that are designed to answer the aforementioned questions are strongly recommended. With such experimental studies, the understanding for the bentonite expansion would improve significantly, resulting in reliable long-term prediction of the EBS performance.

6 CONCLUSIONS

A mathematical model has been established for the bentonite expansion in a planar fracture. Numerical solutions are obtained for the space-time dependent void ratio in the expanding bentonite. A computer code, SABRE, has been developed for the numerical solutions. A fully implicit Galerkin's weighted residual method on deforming elements combined with a predictor-corrector scheme has been applied. The code has been verified by comparing the numerical results with the analytical solution for early times. Then, the numerical results obtained by the code for the experimental conditions have been compared with the already reported experimental results.

The following conclusions are derived:

- By the comparison with the analytical solution for the constant coefficient and early times, it is considered that the governing equations (30), (31), and (41) developed in this study have been properly implemented into the numerical code, SABRE.
- Numerical simulations by the code, SABRE, give a close agreement with the experimental results by assuming that the void ratio at the tip is constant at 4.05 and the void ratio dependencies for the permeability and the compressibility coefficient as in case 3.
- The model has been established based on a number of assumptions. To finally validate the model, it is strongly recommended that the spatial profiles of the void ratio in the expanding bentonite are measured for different times.

7 REFERENCES

[1] K. Terzaghi, Erdbaumechanik auf bodenphysikalischer Grundlage, Leipzig und Wien, F. Deuticke, 1925.

[2] T. Kanno and H. Wakamatsu, Experimental study on bentonite gel migration from a deposition hole, RECOD 91

[3] Power reactor and Nuclear Fuel Development Corporation, Evaluation of extrusion of bentonite buffer (I), PNC TN8410 97-313, 1997.

[4] T. N. Narashimhan and P. A. Witherspoon, Numerical Model for Saturated-Unsaturated Flow in Deformable Porous Media 1. Theory, *Water Resources Research*, **13**(3) 657-664, 1977.

[5] H. Darcy, Détermination des lois d'écoulement de l'eau à travers le sable. Les fontaines publiques de la ville de Dijon, pp. 590-594. Paris : Victor Dalmont, 1856.

[6] A. W. Bishop, The Principle of Effective Stress, *Publ.* 32, Norwegian Geotech. Inst., Oslo, Norway (1960).

[7] K. Terzaghi, R. B. Peck, and G. Mesri, *Soil Mechanics in Engineering Practice*, 3rd ed., Wiley-Interscience, 1996.

[8] P. M. Gresho, R.L. Lee, R.L. Sani, *Recent Advances in Numerical Methods in Fluids,* Pineridge Press, 1980.

[9] H. S. Carlslow and J. C. Jaeger, *Conduction of Heat in Solids*, 2nd Ed., Oxford University Press, 1959.

APPENDIX

MANUAL

FOR

SABRE 4

A.INTRODUCTION.....3

B.GOVERNING EQUATIONS AND SIDE-CONDITIONS 3

C.NUMERICAL METHOD.....5

D.OVERVIEW OF PROGRAM STRUCTURE AND EXECUTION.....7

E.PREPARATION OF INPUT FILES.....9

MATCONST.INP: MATERIAL PROPERTIES.....10
NUMINT.INP: NUMERICAL INTEGRATION PARAMETERS.....11
NODES.INP: GEOMETRICAL DEFINITION.....12
MESH REFINEMENT TO IMPROVE THE SOLUTION.....13
RESTART.INP.....14

F.OUTPUT FILES FROM SABRE.....15

ENODE.OUT.....15
RPLOT.OUT.....16
PLOT.OUT.....16
NEXTRUN.OUT.....17

G.SAMPLE PROBLEM.....18

A. INTRODUCTION

SABRE is a one-dimensional numerical model for simulating the expansion of a cylindrical volume of saturated porous material contacted with water. The motivation for SABRE is to determine the radial expansion of a cylindrical volume of clay contacted with water. The acronym "SABRE" stands for "**sa**turated **b**entonite **r**adial **e**xpansion".

The model on which the code SABRE is based is derived from the consolidation theory developed by Terzaghi.[1] The governing equations are based on two mass conservation laws which account for water flow via Darcy's law.[2]

This manual gives a brief technical description of the code SABRE, including discussions of the material properties modeled, governing equations, numerical methods and code architecture. We also provide instructions for preparing input files, and present a number of illustrative problems.

B. GOVERNING EQUATIONS AND SIDE-CONDITIONS

The geometry is defined as shown in Figure B.1: saturated bentonite initially contained in a cylinder of radius $R(0)$ expands in a horizontal fracture of width L. The bentonite is surrounded by free water in such a way that water absorption occurs only at the location of the tip $R(t)$ of the bentonite. We assume axial symmetry and no z-dependency in the fracture.

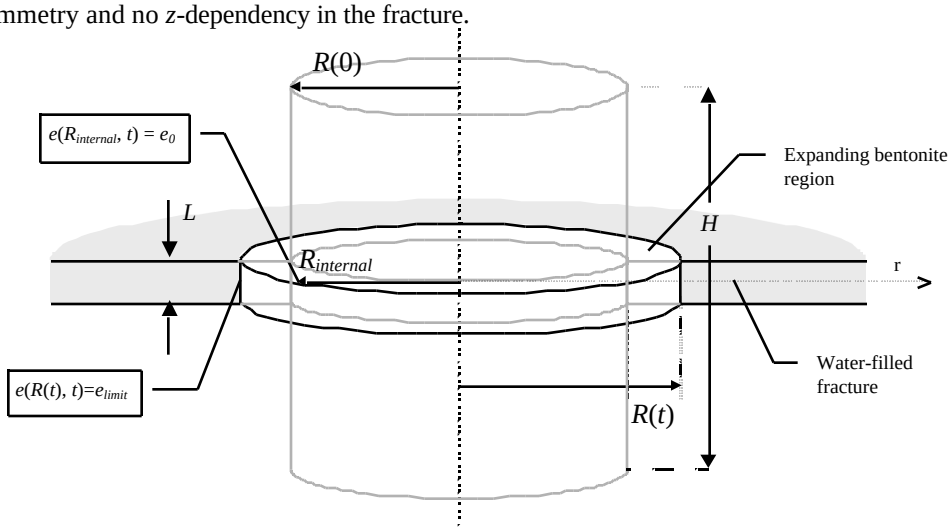

Figure B.1 Geometrical definition of the bentonite volume expanding in the fracture and boundary conditions.

The governing equation is written as

$$\frac{1}{1+e}\frac{\partial e}{\partial t} = \frac{C}{r}\frac{\partial}{\partial r}\left(r \exp(Ge)\frac{\partial e}{\partial r}\right) \text{ on } R_{internal} \le r \le R(t). \tag{A.1}$$

The void ratio $e(r,t)$ in (A.1) has to be solved on the domain $R_{internal} \le r \le R(t)$ where $R(t)$ is given by (A.6), subject to the side conditions, (A.2), (A.3), and (A.4). The lower bound of the bentonite region, $R_{internal}$ is set to be slightly smaller than $R(0)$ in order not to have a zero domain size at the initial time. In general $R_{internal}$ will be taken about 95 % of $R(0)$. The side conditions are

I.C.: $$e(r,0) = e_0 \text{ for } R_{internal} \le r \le R(0), \tag{A.2}$$

B.C.: $$e(R_{\text{internal}},t) = e_0 \text{ for } t > 0, \text{ and} \tag{A.3}$$

$$e(R(t),t) = e_{\text{limit}} \text{ for } t > 0. \tag{A.4}$$

[1] K. Terzaghi, Erdbaumechanik auf bodenphysikalischer Grundlage, Leipzig und Wien, F. Deuticke, 1925.

[2] H. Darcy, Détermination des lois d'écoulement de l'eau à travers le sable. Les fontaines publiques de la ville de Dijon, pp. 590-594. Paris : Victor Dalmont, 1856.

The expression for the position of the moving boundary $R(t)$ as a function of time is written as

$$\frac{d}{dt}\left(\rho_w V_{water}\right) = -A\rho_w \vec{q}\,\vec{n}\Big|_{r=R(t)}, \tag{A.5}$$

where $A = 2\pi R(t)L$ is the surface area of the bentonite in contact with water at the interface bentonite/free water. Introducing Darcy's law as well as the constants C and G given by (A.7) and (A.8), we obtain

$$\frac{dR(t)}{dt} = -C\exp(Ge)\left.\frac{\partial e}{\partial r}\right|_{r=R(t)}. \tag{A.6}$$

In (A.1), the coefficients are defined as

$$C = \frac{2.303\sigma_0' k_0}{\mu C_s}\exp\left[2.303\left(\frac{1}{C_s} - \frac{1}{C_k}\right)\right], \tag{A.7}$$

and

$$G = 2.303\left(\frac{1}{C_k} - \frac{1}{C_s}\right). \tag{A.8}$$

See Eqs. (28) and (29) in Chapter 2 of the main text of this report for functional forms of the permeability and compressibility of the bentonite.

Figure B.2 represents combinations of C and G for which SABRE has been tested successfully, i.e. the results were within 2.5 % around the exact ones. The initial and boundary conditions were R_0 = 0.02 m, e_0 = 0.11 and e_{limit} = 2.7. The range of bentonite initial radii $R(0)$ on which the code SABRE has been successfully tested is [0.02; 10] as given in Figure B.3. The ranges of the void ratios e_0 and e_{limit} on which the code SABRE has been successfully tested are given in Figure B.4.

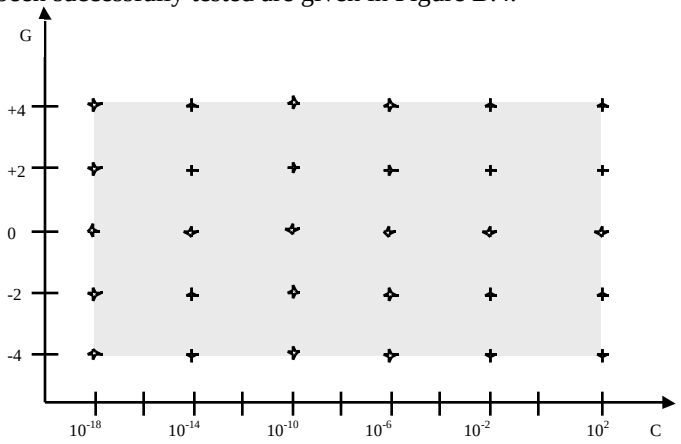

Figure B.2 Values of the parameters C and G where SABRE has been successfully tested. The shaded rectangle represents the ranges of C and G where SABRE is expected to work successfully.

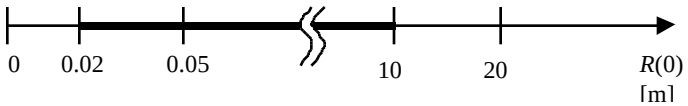

Figure B.3 Range of the initial position of the moving boundary where the code SABRE has been successfully tested.

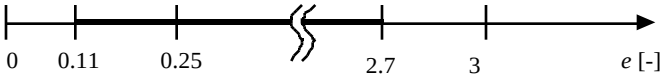

Figure B.4 Ranges of the initial and boundary void ratios where the code SABRE has been successfully tested.

C. NUMERICAL METHOD

The finite element spatial discretization of (A.1), so-called semi-discretization in space, is performed via the Galerkin method, wherein the void ratio $e(r,t)$ is approximated by a sum of N shape functions $\varphi_k(r)$ weighted by N nodal values $e_k(t)$:

$$\tilde{e}(r,t) = \sum_{k=1}^{N} e_k(t)\varphi_k(r) \text{ on } R_{internal} \le r \le R(t), \text{ for } t > 0, \tag{A.9}$$

where $\tilde{e}(r,t)$ denotes a finite dimensional approximation of $e(r,t)$.

The expansion (A.9) of the void ratio is introduced in (A.1), which reads now

$$\frac{C}{r}\frac{\partial}{\partial r}\left[r\exp\left(G\tilde{e}\right)\frac{d\varphi_k}{dr}e_k\right] \approx \frac{1}{1+\tilde{e}}\frac{de_k}{dt}\varphi_k \text{ on } R_{internal} \le r \le R(t),\ t > 0, \tag{A.10}$$

where we used the summation convention introduced by Einstein.

The governing equation (A.10) is multiplied by each of the shape functions $\varphi_i(r)$ and the products are integrated over the space domain bounded by $\Omega(t) = \left[R_{\text{internal}}; R(t)\right]$:

$$\int_{\Omega(t)} \varphi_i\left[\frac{C}{r}\frac{\partial}{\partial r}\left(r\exp\left(G\tilde{e}\right)\frac{d\varphi_k}{dr}e_k\right)\right]2\pi r\,dr = \int_{\Omega(t)} \varphi_i\left[\frac{1}{1+\tilde{e}}\frac{de_k}{dt}\varphi_k\right]2\pi r\,dr\ . \tag{A.11}$$

where $R_{internal} \le r \le R(t)$, $t > 0$, the integrals are set equal for $1 \le i \le N$. By integration by parts of the left hand side,

$$\left[\int_{\Omega(t)} \varphi_i\frac{1}{1+\tilde{e}}\varphi_k r\,dr\right]\dot{e}_k + \left[\int_{\Omega(t)} Cr\exp\left(G\tilde{e}\right)\frac{d\varphi_i}{dr}\frac{d\varphi_k}{dr}\,dr\right]e_k = \left[C\varphi_i r\exp\left(G\tilde{e}\right)\frac{d\varphi_k}{dr}e_k\right]_{r=R_{\text{internal}}}^{r=R(t)} \tag{A.12}$$

where the dot symbol denotes the derivative with respect to time, $R_{internal} \le r \le R(t)$, $t > 0$, $1 \le i \le N$. The result of the above (A.12) "weak form" of (A.1) is a coupled system of non-linear, first-order ordinary differential equations in time, which can be written in the following compact matrix form:

$$\underline{\underline{M}}(t)\,\underline{\dot{e}}(t) + \underline{\underline{K}}(t)\underline{e}(t) = \underline{F}(t) \tag{A.13}$$

We determine the motion of the moving boundary by

$$\dot{R} = C\exp\left(G\tilde{e}\right)\left.\frac{d\varphi_k}{dr}\right|_{r=R(t)} e_k\ , \text{ for } t > 0. \tag{A.14}$$

The internal node motion remains to be defined. We use the following simple law of motion for a node m:

$$r_m(t) = R_{\text{internal}} + c_m R(t) \text{ for } t > 0, \tag{A.15}$$

where c_m are constants, $1 \le m \le N$.

We solve (A.13) and (A.14) in a decoupled fashion. The integration scheme developed here is based on two second-order-accurate integration techniques proposed by Gresho *et al.*,[3] the explicit Adams-Bashforth formula and the implicit trapezoid rule. By combination of these two common techniques, a stable scheme is obtained in which the temporal accuracy is controlled by automatic time step modification based on a good estimate of the local single step time truncation error. This automatic time step modification provides a cost-effective algorithm in the sense that the time step is increased whenever possible and decreased only when necessary. The non-linear systems obtained are solved using a Newton-Raphson method, which requires the construction of a linear system. This unsymmetrical linear system is solved via Gaussian elimination.

The overall time integration scheme can be described as follows. From the knowledge of the moving boundary position and the void ratio at time t_n, we predict the moving boundary position and the void ratio at time t_{n+1}. We then solve (A.13) in the predicted domain and finally, we correct the moving bound-

[3] P.M. Gresho, R.L. Lee, R.L. Sani, Recent Advances in Numerical Methods in Fluids, Pineridge Press, 1980.

ary position by solving (A.14).

More precisely, let $\underline{e}^n$ and R^n be the nodal vector of the void ratio and position of the moving boundary at the time t_n. We obtain the corresponding vector and position at time $t_{n+1}=t_n+\Delta t_n$ after completion of the following steps:

We predict $\underline{e}_{pred}$ and R_{pred} at the time t_{n+1} by means of the variable step, second-order Adams-Bashforth formula. Applied to $\dot{y} = f$, it reads

$$y_{pred}^{N+1} = y^n + \frac{\Delta t_n}{2}\left[2 + \frac{\Delta t_n}{\Delta t_{n-1}}\right]\dot{y}^n - \frac{\Delta t_n}{\Delta t_{n-1}}\dot{y}^{n-1}, \tag{A.16}$$

where the time derivatives $\underline{\dot{y}}^n$ and $\dot{y}^{n-1}$ are known from the previous time steps, $\Delta t_n=t_{n+1}-t_n$.

The internal nodes are relocated by means of the predicted tip position and the law of motion (A.15).

The $\underline{e}^{n+1}$ are computed on the predicted finite-element grid by means of the completely stable implicit Trapezoid rule (Crank-Nicholson). Applied to $\dot{y} = f$, it reads

$$y^{n+1} = y^n + \frac{\Delta t_n}{2}\left(f_n + f_{n+1}\right). \tag{A.17}$$

For a system which is discretized into N grid blocks, (A.17) represents a set of N nonlinear algebraic equations $\underline{\underline{A}}(\underline{x})\underline{x}=\underline{b}(\underline{x})$. Calculation of the void ratio field based on this system of equations is the most costly operation in terms of computer time for it involves the solution of a large nonlinear system. We solve it by the Newton-Raphson iterative technique with predicted values of e and R as first estimates. The solution of the system usually does not require more than one iteration.

We correct the moving boundary position R with the Trapezoid rule (A.17) above.

The time derivatives to be used in the predictor step at the next time step have to be evaluated. This is conveniently done by inversion of the Trapezoid rule:

$$\dot{y}^{n+1} = \frac{2}{\Delta t_n}\left(y^{n+1} - y^n\right) - \dot{y}^n, \tag{A.18}$$

where $\dot{y}^n$ is available from the previous application of the same equation.

An automatic selection of the time increment is made during the simulation, on the basis of the difference between the predicted and corrected values and user-specified level of local time truncation error ε. The default convergence criterion is 10^{-3}. It reads

$$\Delta t_{n+1} = \Delta t_n \left[\frac{\varepsilon}{\left|d\left(y^{n+1}\right)\right|}\right]^{1/\beta} \tag{A.19}$$

where

$$\left|d\left(y^{n+1}\right)\right|^2 = \frac{1}{N+1}\frac{1}{\left[3\left(1+\frac{\Delta t_{n-1}}{\Delta t_n}\right)\right]^2}\left[\frac{1}{\left(e_{\max}^{n+1}\right)^2}\sum_{i=1}^{N}\left(e_i^{n+1} - e_{i,pred}^{n+1}\right)^2 + \frac{1}{\left(R^{n+1}\right)^2}\left(R^{n+1} - R_{pred}^{n+1}\right)^2\right] \tag{A.20}$$

The entire algorithm for advancing the solution by one time step can be summarized as follows:

1. the predictors for the nodal vector of the void ratio and the moving boundary position are computed,
2. the internal nodes are relocated,
3. the system of equations (A.17) is build by looping through the N finite-elements,
4. the nodal vector of the void ratio is computed by solving the linear system,
5. the position of the moving boundary is corrected,
6. the nodal vector of the void ratio change rate and the change rate of the moving boundary position is computed for the next time step,
7. the next time step is computed.

Since $\underline{\dot{e}}^{n-1}$ and $\dot{R}^{n-1}$ are required in the equations (A.16) and (A.18), the method above can not be applied until the third time step. The two first time steps require a special treatment.

D. OVERVIEW OF PROGRAM STRUCTURE AND EXECUTION

The subroutines and functions contained in SABRE can be grouped according to their functions as summarized in Table D.1. Figure D.1 gives an abbreviated overview of the computational procedure (flow chart).

Table D.1 SABRE Program Structure.

Function	Subroutine(s) and Function(s)
data input	OPENNODE, OPENNUM, OPENMAT
keyboard data input	CHOICES, OPTION1
assembling of equations	JABASSEM
computation of local matrices	KLOC, LLOC, MLOC, NLOC
shape functions	TAU1, TAU2
derivatives of shape functions	DTAU1, DTAU2
solution of equations	TRIDAG
output of results	OPENNEXT, OPENREST, RPLOT, PLOT

As we can observe in Figure D.1, SABRE offers four different options at the beginning:
[1] Run the code with new values,
[2] Continue a previous run using the variables in the file RESTART.INP,
[3] Plot the tip position as a function of time using the file ENODE.OUT,
[4] Plot the void ratio distribution at a given time using the file ENODE.OUT.

The execution of the main program in the cases of options 1 or 2 will be commented in this paragraph. The initialization of a simulation is accomplished by the subroutines OPENNODE, which reads the mesh geometry file NODES.INP, OPENNUM which reads the numerical integration parameters in the file NUMINT.INP and OPENMAT which reads the material constants in MATCONST.INP. Then, data are input by the user on the keyboard in CHOICES and OPTION1 (in the case option 1 is chosen). If the code has to start from previous results (option 2), the file RESTART.INP is read in the subroutine OPENREST. Some variables are then initialized. In the case of option 1, SABRE stores the initial time, the initial tip position and the nodal values of the finite-element approximation of the initial void ratio in the file ENODE.OUT before the first time step. The 'time marching process' loop is located in the main program. The function which performs the predictor step is PRED. The internal nodes are relocated in the main program. The elements of the matrices $\underline{\underline{K}}$, $\underline{\underline{L}}$, $\underline{\underline{M}}$ and $\underline{\underline{N}}$ (Eq. (67) in Chapter 3 of the main text) are integrals which are evaluated over the N-2 finite-elements. Each of these numerical integrations is performed on the parent element in the subroutines KLOCALE, LLOCALE, MLOCALE and NLOCALE respectively. The matrices $\underline{\underline{K}}$, $\underline{\underline{L}}$, $\underline{\underline{M}}$ and $\underline{\underline{N}}$ are then assembled in the subroutine JABASSEM. The linear system of N-2 equations is solved using the subroutine TRIDAG. The convergence criterion on the Newton-Raphson iterative scheme for the void ratio is based on the norm of the vector of the relative error between two successive iterations and has to be less than 0.1ε. This norm is given by the function ERROR2. If the convergence criterion is not fulfilled, the program proceeds to another iteration with the most recent nodal values of the void ratio. The function DR computes the relative difference between R^{iter+1} and R^{iter}. The same convergence criterion as on the void ratio is applied to this difference. If it is not fulfilled, SABRE goes back to the calculation of the matrices $\underline{\underline{K}}$, $\underline{\underline{L}}$, $\underline{\underline{M}}$ and $\underline{\underline{N}}$ on the most recent domain $[R_{internal};\ R^{iter+1}]$ with the most recent nodal values of the void ratio and proceeds to another iteration. Afterwards, the function ACCFIELD computes the time derivatives. The function DTNEW computes the new time step. Concerning the time step modification, SABRE always accepts the increase if $\Delta t_{n+1} \geq 0.8\ \Delta t_n$ but repeats the time step with $\Delta t_n = \Delta t_{n+1}$ otherwise. The storage of the variables time, initial tip position and nodal values of the void ratio is performed every *Nskip* time steps. The printout to the screen of the time step and the percentage to complete the expansion is performed every 100 time steps. The simulation proceeds until it terminates for one of several termination criteria input in CHOICES (number of time steps, simulation time, final radius reached). At that time, the storage of the necessary variables in the disk file NEXTRUN.OUT for ulterior runs is performed in the subroutine OPENNEXT. SABRE then proposes to prepare some files to plot either the tip position as a function of time by means of the subroutine RPLOT, or the void ratio as a function of the radius by means of the subroutine PLOT.

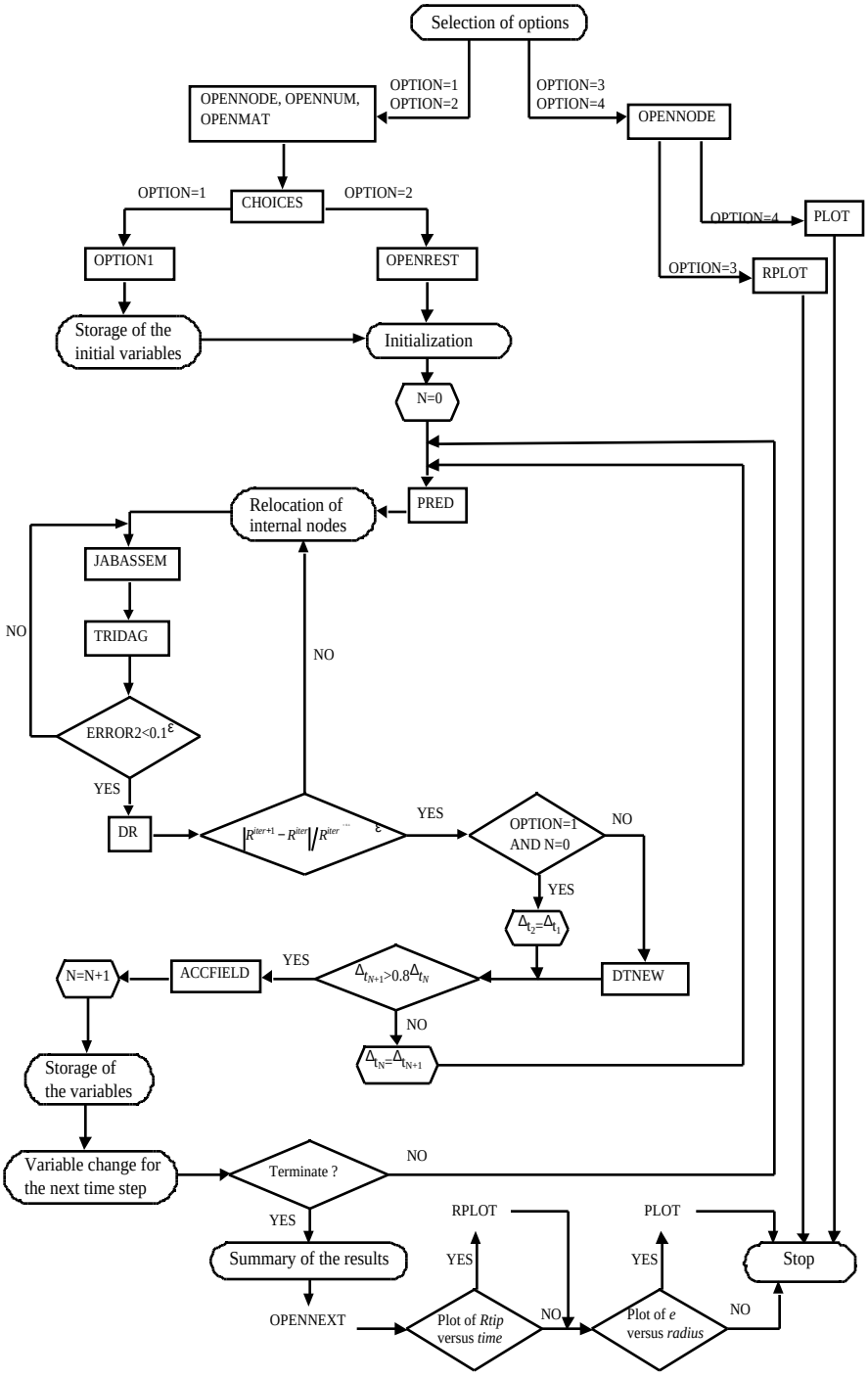

Figure D.1 Simplified flow chart of SABRE.

The first and second time steps in the cases of option 1 require a special treatment which is detailed in (Section 3.3 of the main text).

Options 3 and 4 are used to plot a graph of either the tip position versus time or the void ratio versus radius at a given time, based on the data in the output file ENODE.OUT. SABRE reads the input file NODES.INP using the subroutine OPENNODE and then calls either RPLOT or PLOT to generate the output files RPLOT.OUT or PLOT.OUT using the file ENODE.OUT.

E. PREPARATION OF INPUT FILES

The input data of SABRE is organized into groups which correspond to the data groups given in Tables Table E.1 through Table E.4. The input files are summarized in Table E.1. A detailed description of these input files is given further in the text, except for ENODE.OUT which is required to run options 3 and 4. The input data to be input on the keyboard for options 1 and 2 are in Table E.2, as they are in Table E.3 and Table E.4 for the subroutines RPLOT and PLOT. Depending on the option we choose to run SABRE, different input files are required.

Table E.1 Input Data Files

Input file name	Description of the file	Required for option
MATCONST.INP	Material constants	1 & 2
NUMINT.INP	Numerical integration parameters	1 & 2
NODES.INP	Mesh geometry	1, 2, 3 & 4
RESTART.INP	Restart file	2
ENODE.OUT	Main output file of options 1 & 2	3 & 4

Table E.2 Input Data Specific to Options 1 & 2.

Input data group	Description	Required for option
NSTEP, EXPTIME or RFINAL	Number of time steps, expansion time or final position of the moving boundary	1 & 2
NSKIP	Storage of the variables in ENODE.OUT every NSKIP time steps	1 & 2
DELTAT	First time step	1
RTIPINIT	Initial position of the moving boundary	1
EINITIAL	Initial void ratio	1
BC	Void ratio at the moving boundary	1
RESTART.INP	Restart input file	2

Remarks on Table E.2:

Item 1: NSTEP, EXPTIME or RFINAL. SABRE offers three different options concerning the period of time of bentonite expansion:
[1] I want to enter the number of time steps NSTEP performed by the code,
[2] I want to enter the expansion time EXPTIME in seconds,
[3] I want to enter the final tip position in meters.
The differences between options 1, 2 and 3 is that the number of time steps NSTEP, the expansion time EXPTIME or the final tip position RFINAL will be requested later on by the code.

Item 2: NSKIP. Storage of the variables in ENODE.OUT every NSKIP time steps.
SABRE asks every how many time steps the nodal values of the void ratio have to be stored in the output file ENODE.OUT. The output file ENODE.OUT is the most important one generated by the code SABRE and can become very long. The variables time, tip position and nodal values of the void ratio are stored in this output file according to the format described in the next chapter. In order not to generate a too long output file ENODE.OUT, the code offers the possibility of storing these variables every x time steps. This proves very useful especially in the case the run requested by the user requires several hundreds of iterations. It also accelerates the code by decreasing the number of times the hard drive has to be accessed.

Item 3: DELTAT. First time step.
The code will fail for too large values of the first time step Δt_0. It is recommended to run calculations with a first time step of approximately 14 orders of magnitude smaller than the time scale of the expansion. Too small first time steps may lead to longer runs. The time scale of the expansion will depend on the material parameters C and G. Since the time scale is proportional to C, the time scale will decrease for larger C's. The time scale also decreases for larger G's. Thus smaller first time steps will have to be chosen accordingly. Figure E.1 gives the first time steps corresponding to different runs within the ranges of C and G. The initial and boundary conditions were $R(0) = 0.02$ m, $e_0 = 0.11$ and $e_{limit} = 2.7$.

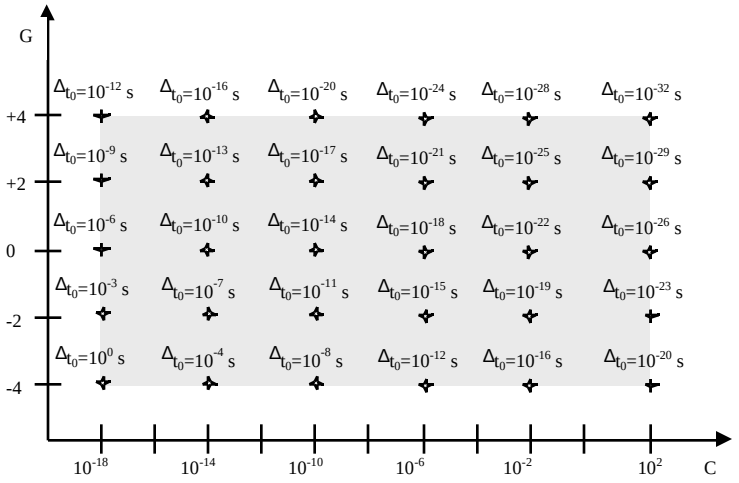

Figure E.1 Influence of *C* and *G* on the first time step, for $R(0) = 0.02$ m, $e_0 = 0.11$ and $e_{limit} = 2.7$

Table E.3 Input data for the subroutine RPLOT.

Input data group	Description	Required for option
CHOICEM	Units of the *y*-axis, which corresponds to the tip position, [1] for meters and [2] for millimeters	3
CHOICER	The tip position is measured from [1] the center of the cylindrical volume or [2] a radius RSPEC to be specified by the user	3
RSPEC	If CHOICER=2, the radius is now to be specified in the units of CHOICEM	3
CHOICET	Units of the *x*-axis, which corresponds to the time, [1] for seconds, [2] for hours, [3] for days and [4] for years	3
CHOICEL	Time scale, [1] for linear, [2] for logarithmic and [3] for square root of time	3

Table E.4 Input data for the subroutine PLOT.

Input data group	Description	Required for option
TIME	Time for which the graph of the void ratio versus radius has to be plotted	4
CHOICEM	Units of the *x*-axis, which corresponds to the radius, [1] for meters and [2] for millimeters	4

Remarks on Table E.4:

Item 1: TIME. Time for which the graph of the void ratio versus radius has to be plotted.
If the user-specified time does not belong to the time range in the file ENODE.OUT, an error message of the type '*The time entered is greater/lower than the upper/lower bound x sec of the time range in the file ENODE.OUT*' will be displayed.

MATCONST.INP: Material properties

SABRE reads the material parameters *C* and *G* in the input file MATCONST.INP. An example of such a file is (see Table I in Page 23 of the main text)

```
90                                   Number of intervals of the void ratio
```

```
0.55      1.27E-10     -0.083005334       the void ratio, C, G
0.60      7.46E-11      0.530868112
0.65      3.55E-11      1.337778449
0.70      1.92E-11      1.888467261
0.75      1.37E-11      2.07228886
0.80      1.28E-11      1.982713731
0.85      1.26E-11      1.858372679
0.90      1.28E-11      1.719078444
0.95      5.72E-11      0.007017558
1.00      5.72E-11      0.007017558
1.05      5.72E-11      0.007017558
1.10      5.72E-11      0.007017558
1.15      5.72E-11      0.007017558
1.20      5.72E-11      0.007017558
1.25      5.72E-11      0.007017558
1.30      5.72E-11      0.007017558
```

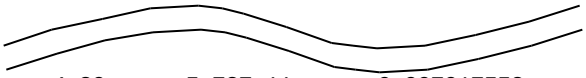

```
4.30      5.72E-11      0.007017558
4.35      5.72E-11      0.007017558
4.40      5.72E-11      0.007017558
4.45      5.72E-11      0.007017558
4.50      5.72E-11      0.007017558
4.55      5.72E-11      0.007017558
4.60      5.72E-11      0.007017558
4.65      5.72E-11      0.007017558
4.70      5.72E-11      0.007017558
4.75      5.72E-11      0.007017558
4.80      5.72E-11      0.007017558
4.85      5.72E-11      0.007017558
4.90      5.72E-11      0.007017558
4.95      5.72E-11      0.007017558
5.00      5.72E-11      0.007017558
```

NUMINT.INP: Numerical integration parameters

Numerical integrations are required in finite-element methods. Analytical integrals are replaced by discrete integrals. Using N_{int} integration points, they read

$$\int_{-1}^{+1} f(\xi) d\xi = \sum_{i=1}^{N\,\mathrm{int}} w_i \, f(\xi_i),$$

where ξ_i are the integration points and vary from –1 to +1, w_i are the integration weights, which vary from 0 to 2. The Gauss-Legendre quadrature sets are commonly used for numerical integrations. The integration points and weights for N_{int}= 2, 4, 8 and 16 are in Table E.5. All examples in this manual are done with 4 integration points.

A couple of properties which are verified by the code SABRE are that the integration points add up to 0 and the integrations weights add up to 2.

In the input file NUMINT.INP, the number of integration points NINT must be entered on the first line; the NINT integration points must be entered on the NINT following lines; the NINT integration weights must be entered on the NINT last lines:

NINT number of integration points, integer variable
KSIINT(I) I=1, …, NINT, integration points, double precision variables
WINT(I)I=1, …, NINT, integration weights, double precision variables

An example of such a file is

```
4                          (number of integration points, integer variable)
-0.861136311594053D0 ⎫
-0.339981043584856D0 ⎬     (integration points, double precision variables)
0.339981043584856D0  ⎪
0.861136311594053D0  ⎭
0.347854845137454D0  ⎫
0.652145154862546D0  ⎬     (integration weights, double precision variables)
0.652145154862546D0  ⎪
0.347854845137454D0  ⎭
```

Table E.5 Gauss-Legendre quadrature sets.

N_{int}	i	ξ_i	w_i
2	1	±0.577350269189626D0	1.000000000000000D0
4	1 & 4	±0.861136311594053D0	0.347854845137454D0
	2 & 3	±0.339981043584856D0	0.652145154862546D0
8	1 & 8	±0.960289856497536D0	0.101228536290376D0
	2 & 7	±0.796666477413627D0	0.222381034453374D0
	3 & 6	±0.525532409916329D0	0.313706645877887D0
	4 & 5	±0.183434642495650D0	0.362683783378363D0
16	1 & 16	±0.989400934991650D0	0.027152459411754D0
	2 & 15	±0.944575023073233D0	0.062253523938648D0
	3 & 14	±0.865631202387832D0	0.095158511682493D0
	4 & 13	±0.755404408355003D0	0.124628971255534D0
	5 & 12	±0.617876244402644D0	0.149595988816577D0
	6 & 11	±0.458016777657227D0	0.169156519395003D0
	7 & 10	±0.281603550779259D0	0.182603415044924D0
	8 & 9	±0.095012509837637D0	0.189450610455067D0

NODES.INP: Geometrical definition

The relative radii c_m defined by (A.15) are constants. For the first and last nodes, they are equal to 0 and 1 respectively. The relative radii of all other nodes are input in strictly increasing order and must belong to the range] 0 ; 1 [.

In the input file NODES.INP, the number of nodes NNODE (integer variable) must be entered on the first line; the NNODE relative radii of the nodes c_m (double precision variables) must be entered on the NNODE following lines.

NNODE number of nodes in the mesh
NODEPOS(I) I=1, …, NNODE, values of the c_i's, double precision variables

An example of such a file is

```
16                (number of nodes, integer variable)
0.000000D0        (relative radius 0 of the first node, double precision
0.200000D0        variable)
0.400000D0
0.600000D0
```

```
0.795300D0
0.897700D0
0.948900D0
0.974500D0        (relative radii of the intermediate nodes, double
0.987300D0        precision variables, in increasing order)
0.993700D0
0.996900D0
0.998500D0
0.999300D0
0.999700D0
0.999900D0
1.000000D0        (relative radius 1 of the last node, double precision
                  variable)
```

Mesh refinement to improve the solution

It is recommended to refine the mesh in case of non-convergence to the theoretical tip position. This is the only way to improve this convergence and the overall accuracy of the code. The reason for this local refinement is the following.

At the time t=0, the void ratio is uniformly equal to e_0. For $t > 0$, the boundary condition imposes $e=e_{limit}$ at the tip $r=R(t)$. Since $e_{limit} \neq e_0$, a singularity is generated by this boundary condition at t=0 and the gradient of the void ratio at $r=R(t)$ tends to infinity as we approach t=0 from positive times. With the finite-element approximation (A.9), the gradient of the void ratio for these early times will be imposed by the mesh size:

$$\lim_{t \to 0} \left. \frac{\partial e}{\partial r} \right|_{r=R(t)} = \frac{e_{\text{limit}} - e_0}{r_N - r_{N-1}} .$$

At early times thus, the only way to have higher values of the gradient at the tip, i.e. a better approximation of the void ratio, is to decrease the mesh size $(r_N - r_{N-1})$.

Since we cannot have too different adjacent meshes, it would be sensible to increase the mesh sizes from the tip $r=R(t)$ to the center r=0 according to

$$(c_k - c_{k-1}) = \alpha (c_{k+1} - c_k) = \alpha^2 (c_{k+2} - c_{k+1}) = \ldots = \alpha^{N-k} (c_N - c_{N-1})$$

where α is the multiplication factor. This geometrical progression imposes increasing mesh sizes from $r=R(t)$ to $r=R(0)$. The positions of the c_k's are given by:

$$c_{k-1} = c_N - (c_N - c_{N-1}) \sum_{j=k}^{N} \alpha^{N-j}$$

In order not to have too large meshes close to $r = R(0)$, a maximum mesh size of 0.20 is also imposed. If the difference between e_{limit} and e_0 increases, the gradient at the tip will be larger and $(c_N - c_{N-1})$ will have to decrease. Several runs have been performed with the following initial conditions:

- initial tip position $R(0)$ = 0.02 m,
- initial void ratio at the tip e_0 = 0.11,

and boundary condition:

- void ratio at the tip e_{limit} = 2.7.

Computations have been performed until the bentonite had completely expanded. According to the results obtained, it seems sensible to build meshes according to the following rules:

- To obtain accurate results, the last mesh size $(c_N - c_{N-1})$ can not be chosen independently on the value of G. For the e_0=0.11 and e_{limit}=2.7 above, $(c_N - c_{N-1})$ has to be taken equal to 10^{-6} for G belonging to the range $[-4.0;-3.0]$, 10^{-5} for $[-3.0;-2.0]$, 10^{-4} for $[-2.0;0.0]$, and 10^{-3} for $[0.0;4.0]$. These ranges are represented in Figure E.2. If the difference between e_{limit} and e_0 decreases, the gradient at the tip will be lower and $(c_N - c_{N-1})$ can increase. If a too small or too large $(c_N - c_{N-1})$ is chosen, the numerical scheme will not converge to the right value.

- The value of $(c_N - c_{N-1})$ will have a strong impact on the CPU time. Indeed, the decrease by a factor 10 of $(c_N - c_{N-1})$ results in an increase by the same factor of the number of iterations or CPU time.
- For given void ratios e_0 and e_{limit}, α will also depend on the value of G. As a general rule, α should be taken equal to 4 for G belonging to the range $[-4.0;-3.0]$, 3 for $[-3.0;0.0]$ and 2 for $[0.0;4.0]$, see Figure E.2.

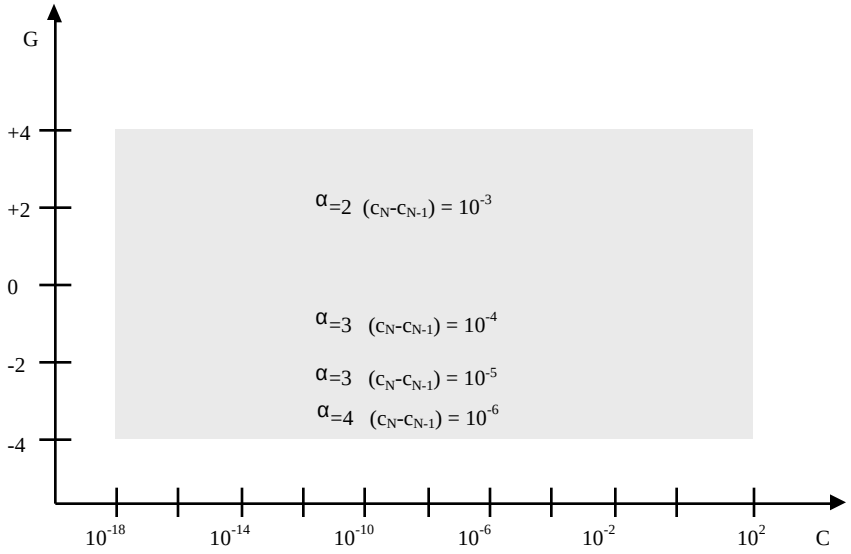

Figure E.2 Influence of *C* and *G* on the parameters α and $(c_N - c_{N-1})$, for e_0 = 0.11 and e_{limit} = 2.7.

RESTART.INP

A new run starting from the end of a previous one can be performed with SABRE. The output file NEXTRUN.OUT from the previous run will have to be copied to or renamed RESTART.INP in order to continue the run starting from the end of the previous one. The format of the input file RESTART.INP is the following:

RCENTER	internal radius of the expanding volume (double precision variable),
RTIPINIT	initial position of the moving boundary (double precision variable),
EINITIAL	initial void ratio (double precision variable),
BC	void ratio at the moving boundary (double precision variable),
TIME	current time (double precision variable),
DELTAPV	previous time step (double precision variable),
DELTAT	new time step (double precision variable),
RTIPPV	previous position of the moving boundary (double precision variable),
RTIPAPV	previous tip position change rate (double precision variable),
RTIPA	current tip position change rate (double precision variable),

and the NNODE consecutive sets of 3 variables, I= 1, …, NNODE, where NNODE is the number of nodes in the mesh and is given in the input file NODES.INP:

ENODEPV(I)	previous nodal values (double precision variables),
ENODEAPV(I)	previous nodal value change rates (double precision variables),
ENODEA(I)	current nodal value change rates (double precision variables).

F. OUTPUT FILES FROM SABRE

SABRE can produce a variety of output files, most of which are controllable by the user. Running the options 1 or 2 of the code will automatically produce the output files ENODE.OUT and NEXTRUN.OUT, and optionally RPLOT.OUT and PLOT.OUT. Running options 3 and 4 will automatically produce the output files RPLOT. This is summarized in Table F.1:

Table F.1 Output files for the problems.

Output file name	Description of the file	Generated by option
ENODE.OUT	Main output containing the time, the tip position and the nodal values of the void ratio	1 & 2
NEXTRUN.OUT	Necessary to restart a run from the state reached at the end of a run	1 & 2
RPLOT.OUT	Contains the tip position as a function of time	3 and optionally 1 & 2
PLOT.OUT	Contains the void ratio as a function of the radius at a user-specified time	4 and optionally 1 & 2

ENODE.OUT

The output file ENODE.OUT contains the position of the tip in meters and the nodal values of the finite-element approximation of the void ratio as a function of time in seconds. The format of the output file ENODE.OUT is a series of the following variables on each line: time, position of the tip , NNODE nodal values of the void ratio. NNODE is the number of nodes in the mesh and is given in the input file NODES.INP:

TIME current time, double precision variable
RTIPNEW current tip position, double precision variable
ENODENEW(I) I=1, …, NNODE, curent nodal values of the void ratio (double precision variables)

This series of variables is stored in the output file ENODE.OUT every NSKIP time steps, where NSKIP is input by the user. In order for the code to detect the end of the file when reading ENODE.OUT, all the variables are set equal to 0 on the last line.

An example of such a file is

```
0.000000000000000E+000  2.000000000000000E-002  1.100000000000000E-001
1.100000000000000E-001  1.100000000000000E-001  1.100000000000000E-001
1.100000000000000E-001  1.100000000000000E-001  1.100000000000000E-001
1.100000000000000E-001  1.100000000000000E-001  1.100000000000000E-001
1.100000000000000E-001  1.100000000000000E-001  1.100000000000000E-001
2.228308336530609       2.137928826957240E-002  1.100000000000000E-001
3.229823914500822E-001  5.876024755291979E-001  9.410248456660871E-001
1.481325296842263       1.868461188948475       2.342133820173359
 2.566480519214161      2.653880084630703       2.684778813255304
 2.695292001839143      2.698817131749035       2.700000000000000
 5.355135919690731      2.224640209304986E-002  1.100000000000000E-001
 3.281751107440636E-001 5.978010538753925E-001  9.554522895892064E-001
 1.497496812530407      1.882649935659595       2.350147666695961
 2.569859923623135      2.655103880431359       2.685189329021096
 2.695420424033066      2.698848691556965       2.700000000000000
 9.926863694905755      2.318617461499974E-002  1.100000000000000E-001
 3.320591299975882E-001 6.050512936510187E-001  9.653544503670982E-001
```

```
1.508441289397609          1.892253555562810          2.355594435886983
2.572159054543686          2.655936535349159          2.685468735624571
2.695507425191599          2.698870237075718          2.700000000000000
16.880560040932890         2.428561269661845E-002     1.100000000000000E-001
3.364400417209572E-001     6.131378392263118E-001     9.762836805604195E-001
1.520393637688638          1.902680477608014          2.361463345290852
2.574625949743068          2.656828327987387          2.685767799475395
2.695600452283654          2.698893543673791          2.700000000000000
0.000000000000000E+000     0.000000000000000E+000     0.000000000000000E+000
0.000000000000000E+000     0.000000000000000E+000     0.000000000000000E+000
0.000000000000000E+000     0.000000000000000E+000     0.000000000000000E+000
0.000000000000000E+000     0.000000000000000E+000     0.000000000000000E+000
0.000000000000000E+000     0.000000000000000E+000     0.000000000000000E+000
```

RPLOT.OUT

The file RPLOT.OUT contains the position of the moving boundary as a function of time. The moving boundary position can be measured either in meters or millimeters, and either from the center of the cylindrical volume or another user-specified radius (see plotting specifications in Table E.3). The time can be measured in seconds, hours, days or years, and the time scale can be linear, logarithmic or square root of time (see plotting specifications in Table E.4). The format of the output file RPLOT.OUT is a series of two variables on each line: time and position of the tip:

TIME	current time, e15.8
RTIP	tip position, e15.8

This series of variables is stored in the output file RPLOT.OUT as many times as the number of time steps stored in the file ENODE.OUT. An example of such a file is

```
.00000000E+00   .20000000E+02   (initial time and tip position)
.11188920E+00   .20325973E+02
.32574906E+00   .20538513E+02
.54387142E+00   .20683533E+02   (beginning of the file RPLOT.OUT)
.76685093E+00   .20803749E+02
.99509118E+00   .20911489E+02
.12289474E+01   .21011938E+02
```

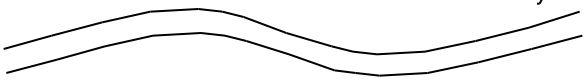

```
.16692030E+03   .34179745E+02
.17232083E+03   .34404231E+02
.17780763E+03   .34628371E+02
.18337806E+03   .34852061E+02   (end of the file RPLOT.OUT)
.18902943E+03   .35075205E+02
.19475905E+03   .35297711E+02
.20056423E+03   .35519495E+02   (final time and tip position)
```

PLOT.OUT

The file PLOT.OUT contains the nodal values of the finite-element approximation of the void ratio as a function of the radius at a time input by the user. The radius can be measured either in meters or millimeters (see plotting specifications in Table E.4). The format of the output file PLOT.OUT is a series of two variables on each line: radius and nodal value of the finite-element approximation of the void ratio at this radius. There are 501 lines in the output file PLOT.OUT, I=1, …, 501, corresponding to 501 equidistant radial positions:

RPOS(I) radius, e15.8
E(I) tip position, e15.8

An example of such a file is

```
  .19000000E+02   .11000000E+00   (first radius r=0 and nodal value)
  .19031433E+02   .11264075E+00
  .19062866E+02   .11528151E+00   (beginning of the file PLOT.OUT)
  .19094298E+02   .11792226E+00
  .19125731E+02   .12056301E+00
  .19157164E+02   .12320377E+00
```

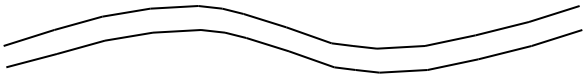

```
  .26732473E+02   .85600480E+00
  .26763906E+02   .85983576E+00
  .26795339E+02   .86366672E+00
  .26826772E+02   .86749767E+00
  .26858205E+02   .87132863E+00   (middle of the file PLOT.OUT)
  .26889637E+02   .87515959E+00
  .26921070E+02   .87899055E+00
  .26952503E+02   .88282151E+00
  .26983936E+02   .88665247E+00
```

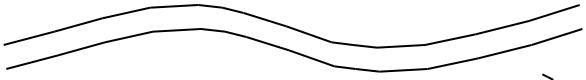

```
  .34559245E+02   .26103052E+01
  .34590678E+02   .26278730E+01
  .34622111E+02   .26454408E+01   (end of the file PLOT.OUT)
  .34653543E+02   .26630085E+01
  .34684976E+02   .26813980E+01
  .34716409E+02   .27000000E+01   (tip position r=R(TIME) and
                                   nodal value at the tip)
```

NEXTRUN.OUT

As explained in the previous chapter, the code stores enough information in the output file NEXTRUN.OUT to be able to perform a new run starting from the state reached so far. The output file NEXTRUN.OUT will have to be copied to or renamed RESTART.INP in order to continue a run using option 2 of SABRE. The format of the input file NEXTRUN.OUT is the following:

RCENTER internal radius of the expanding volume (double precision variable),
RTIPINIT initial position of the moving boundary (double precision variable),
EINITIAL initial void ratio (double precision variable),
BC void ratio at the moving boundary (double precision variable),

TIME current time (double precision variable),
DELTAPV previous time step (double precision variable),
DELTAT new time step (double precision variable),

RTIPPV previous position of the moving boundary (double precision variable),
RTIPAPV previous tip position change rate (double precision variable),
RTIPA current tip position change rate (double precision variable),

and the NNODE consecutive sets of 3 variables, I= 1, …, NNODE, where NNODE is the number of nodes in the mesh and is given in the input file NODES.INP:

ENODEPV(I) previous nodal values (double precision variables),
ENODEAPV(I) previous nodal value change rates (double precision variables),
ENODEA(I) current nodal value change rates (double precision variables).

G. SAMPLE PROBLEMS

An example problem set up here is as follows. The radius of the bentonite is 1.0 m initially. The initial bentonite void ratio is 0.5. The tip void ratio is 4.0.

The data-input window looks as follows: (***bold italic*** is the value typed in.)

```
*******************************************************************************
*************** SABRE : Saturated Bentonite Radial Expansion ******************
*******************************************************************************

Enter the number between brackets which corresponds to your choice :
[1] Run the code with new values,
[2] Continue a previous run using the variables in the file 'restart.inp',
[3] Plot the tip position as a function of time using the file 'enode.out',
[4] Plot the void ratio distribution at a given time using the file 'enode.out'.
1

******************** Reading of the input parameters files *******************
Reading of the mesh definition in the file 'nodes.inp'.

The total number of nodes is 12.

Reading of the numerical integration parameters in the file 'numint.inp'.

The number of integration points is 4.

Reading of the material constants in the file 'matconst.inp'.
   0.600000000000000       7.460000000000001D-11    0.530868112000000
   0.650000000000000       3.550000000000000D-11    1.33777844900000
   0.700000000000000       1.920000000000000D-11    1.88846726100000
   0.750000000000000       1.370000000000000D-11    2.07228886000000
   0.800000000000000       1.280000000000000D-11    1.98271373100000
   0.850000000000000       1.260000000000000D-11    1.85837267900000
   0.900000000000000       1.280000000000000D-11    1.71907844400000
   0.950000000000000       5.720000000000000D-11   7.017558000000000D-03
    1.00000000000000       5.720000000000000D-11   7.017558000000000D-03
    1.05000000000000       5.720000000000000D-11   7.017558000000000D-03
    1.10000000000000       5.720000000000000D-11   7.017558000000000D-03
    1.15000000000000       5.720000000000000D-11   7.017558000000000D-03
    1.20000000000000       5.720000000000000D-11   7.017558000000000D-03
    1.25000000000000       5.720000000000000D-11   7.017558000000000D-03
    1.30000000000000       5.720000000000000D-11   7.017558000000000D-03
    1.35000000000000       5.720000000000000D-11   7.017558000000000D-03
    1.40000000000000       5.720000000000000D-11   7.017558000000000D-03
    1.45000000000000       5.720000000000000D-11   7.017558000000000D-03
    1.50000000000000       5.720000000000000D-11   7.017558000000000D-03
    1.55000000000000       5.720000000000000D-11   7.017558000000000D-03
    1.60000000000000       5.720000000000000D-11   7.017558000000000D-03
    1.65000000000000       5.720000000000000D-11   7.017558000000000D-03
    1.70000000000000       5.720000000000000D-11   7.017558000000000D-03
    1.75000000000000       5.720000000000000D-11   7.017558000000000D-03
    1.80000000000000       5.720000000000000D-11   7.017558000000000D-03
```

1.850000000000000	5.720000000000000D-11	7.017558000000000D-03
1.900000000000000	5.720000000000000D-11	7.017558000000000D-03
1.950000000000000	5.720000000000000D-11	7.017558000000000D-03
2.000000000000000	5.720000000000000D-11	7.017558000000000D-03
2.050000000000000	5.720000000000000D-11	7.017558000000000D-03
2.100000000000000	5.720000000000000D-11	7.017558000000000D-03
2.150000000000000	5.720000000000000D-11	7.017558000000000D-03
2.200000000000000	5.720000000000000D-11	7.017558000000000D-03
2.250000000000000	5.720000000000000D-11	7.017558000000000D-03
2.300000000000000	5.720000000000000D-11	7.017558000000000D-03
2.350000000000000	5.720000000000000D-11	7.017558000000000D-03
2.400000000000000	5.720000000000000D-11	7.017558000000000D-03
2.450000000000000	5.720000000000000D-11	7.017558000000000D-03
2.500000000000000	5.720000000000000D-11	7.017558000000000D-03
2.550000000000000	5.720000000000000D-11	7.017558000000000D-03
2.600000000000000	5.720000000000000D-11	7.017558000000000D-03
2.650000000000000	5.720000000000000D-11	7.017558000000000D-03
2.700000000000000	5.720000000000000D-11	7.017558000000000D-03
2.750000000000000	5.720000000000000D-11	7.017558000000000D-03
2.800000000000000	5.720000000000000D-11	7.017558000000000D-03
2.850000000000000	5.720000000000000D-11	7.017558000000000D-03
2.900000000000000	5.720000000000000D-11	7.017558000000000D-03
2.950000000000000	5.720000000000000D-11	7.017558000000000D-03
3.000000000000000	5.720000000000000D-11	7.017558000000000D-03
3.050000000000000	5.720000000000000D-11	7.017558000000000D-03
3.100000000000000	5.720000000000000D-11	7.017558000000000D-03
3.150000000000000	5.720000000000000D-11	7.017558000000000D-03
3.200000000000000	5.720000000000000D-11	7.017558000000000D-03
3.250000000000000	5.720000000000000D-11	7.017558000000000D-03
3.300000000000000	5.720000000000000D-11	7.017558000000000D-03
3.350000000000000	5.720000000000000D-11	7.017558000000000D-03
3.400000000000000	5.720000000000000D-11	7.017558000000000D-03
3.450000000000000	5.720000000000000D-11	7.017558000000000D-03
3.500000000000000	5.720000000000000D-11	7.017558000000000D-03
3.550000000000000	5.720000000000000D-11	7.017558000000000D-03
3.600000000000000	5.720000000000000D-11	7.017558000000000D-03
3.650000000000000	5.720000000000000D-11	7.017558000000000D-03
3.700000000000000	5.720000000000000D-11	7.017558000000000D-03
3.750000000000000	5.720000000000000D-11	7.017558000000000D-03
3.800000000000000	5.720000000000000D-11	7.017558000000000D-03
3.850000000000000	5.720000000000000D-11	7.017558000000000D-03
3.900000000000000	5.720000000000000D-11	7.017558000000000D-03
3.950000000000000	5.720000000000000D-11	7.017558000000000D-03
4.000000000000000	5.720000000000000D-11	7.017558000000000D-03
4.050000000000000	5.720000000000000D-11	7.017558000000000D-03
4.100000000000000	5.720000000000000D-11	7.017558000000000D-03
4.150000000000000	5.720000000000000D-11	7.017558000000000D-03
4.200000000000000	5.720000000000000D-11	7.017558000000000D-03
4.250000000000000	5.720000000000000D-11	7.017558000000000D-03
4.300000000000000	5.720000000000000D-11	7.017558000000000D-03
4.350000000000000	5.720000000000000D-11	7.017558000000000D-03
4.400000000000000	5.720000000000000D-11	7.017558000000000D-03
4.450000000000000	5.720000000000000D-11	7.017558000000000D-03
4.500000000000000	5.720000000000000D-11	7.017558000000000D-03
4.550000000000000	5.720000000000000D-11	7.017558000000000D-03
4.600000000000000	5.720000000000000D-11	7.017558000000000D-03

```
    4.65000000000000       5.720000000000000D-11   7.017558000000000D-03
    4.70000000000000       5.720000000000000D-11   7.017558000000000D-03
    4.75000000000000       5.720000000000000D-11   7.017558000000000D-03
    4.80000000000000       5.720000000000000D-11   7.017558000000000D-03
    4.85000000000000       5.720000000000000D-11   7.017558000000000D-03
    4.90000000000000       5.720000000000000D-11   7.017558000000000D-03
    4.95000000000000       5.720000000000000D-11   7.017558000000000D-03
    5.00000000000000       5.720000000000000D-11   7.017558000000000D-03

****************** Input parameteres files successfully read ******************
Enter the number between brackets which corresponds to your choice :
[1] I want to enter the number of time steps performed by the code,
[2] I want to enter the expansion time in seconds,
[3] I want to enter the final tip position in meters.
2

Expansion time [sec] :  1.0e9

Every how many time steps do you want the void ratio to be stored in the output
file 'enode.out':  1000

First time step [sec] :  1.0e-10

Internal radius of the expanding volume [m] :  1.0

***************************** Initial conditions ******************************
Initial position of the moving boundary [m] :  1.01

Initial void ratio [-] :  0.5

***************************** Boundary condition ******************************
Void ratio at the moving boundary [-] :  4.0

Creation of the file 'enode.out' where the position of the moving boundary as well
as the nodal values of the finite-element approximation of the void ratio will be
stored as a function of time.

The format of this file is, on each line : 'time' (double precision variable),
'position of the moving boundary' (double precision variable) and 'nodal values of
the finite-element approximation of the void ratio' (12 double precision
variables).

***************************** SABRE is computing ******************************
Time =  2.77778E-14 hour, Time step :        1, tip position :  1.01000000E+00 m.
Time =  5.55556E-14 hour, Time step :        2, tip position :  1.01000000E+00 m.
Time =  2.38120E-07 hour, Time step :        3, tip position :  1.01000017E+00 m.
Time =  5.67804E-07 hour, Time step :        4, tip position :  1.01000040E+00 m.
Time =  1.53376E-06 hour, Time step :        5, tip position :  1.01000096E+00 m.
Time =  2.64104E-06 hour, Time step :        6, tip position :  1.01000145E+00 m.
Time =  3.99411E-06 hour, Time step :        7, tip position :  1.01000190E+00 m.
Time =  6.03187E-06 hour, Time step :        8, tip position :  1.01000239E+00 m.
Time =  7.73186E-06 hour, Time step :        9, tip position :  1.01000271E+00 m.
Time =  9.54735E-06 hour, Time step :       10, tip position :  1.01000301E+00 m.
```

```
Time =  9.79679E-02 hour, Time step :      100, tip position :  1.01036721E+00 m.
Time =  2.78107E-01 hour, Time step :      200, tip position :  1.01064521E+00 m.
Time =  5.10581E-01 hour, Time step :      300, tip position :  1.01087326E+00 m.
Time =  7.97520E-01 hour, Time step :      400, tip position :  1.01106591E+00 m.
Time =  1.14079E+00 hour, Time step :      500, tip position :  1.01124581E+00 m.
Time =  1.54219E+00 hour, Time step :      600, tip position :  1.01142669E+00 m.
Time =  2.00353E+00 hour, Time step :      700, tip position :  1.01160976E+00 m.
Time =  2.52670E+00 hour, Time step :      800, tip position :  1.01179455E+00 m.
Time =  3.11367E+00 hour, Time step :      900, tip position :  1.01198180E+00 m.
Time =  3.76643E+00 hour, Time step :     1000, tip position :  1.01217211E+00 m.
```

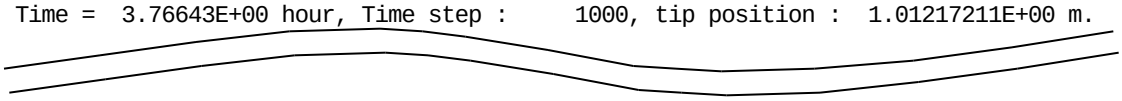

```
Time =  7.74889E+02 hour, Time step :    10000, tip position :  1.03812843E+00 m.
```

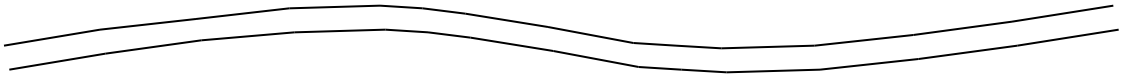

```
Time =  2.74347E+05 hour, Time step :   119900, tip position :  1.59969262E+00 m.
Time =  2.74648E+05 hour, Time step :   120000, tip position :  1.60000253E+00 m.
Time =  2.74949E+05 hour, Time step :   120100, tip position :  1.60031232E+00 m.
Time =  2.75250E+05 hour, Time step :   120200, tip position :  1.60062198E+00 m.
Time =  2.75551E+05 hour, Time step :   120300, tip position :  1.60093151E+00 m.
Time =  2.75852E+05 hour, Time step :   120400, tip position :  1.60124091E+00 m.
Time =  2.76153E+05 hour, Time step :   120500, tip position :  1.60155018E+00 m.
Time =  2.76454E+05 hour, Time step :   120600, tip position :  1.60185932E+00 m.
Time =  2.76756E+05 hour, Time step :   120700, tip position :  1.60216833E+00 m.
Time =  2.77057E+05 hour, Time step :   120800, tip position :  1.60247721E+00 m.
Time =  2.77358E+05 hour, Time step :   120900, tip position :  1.60278597E+00 m.
Time =  2.77660E+05 hour, Time step :   121000, tip position :  1.60309459E+00 m.

************************** The computations are done **************************

The expansion time is  0.10000093E+10 sec.
The number of time steps is   121040.
The number of time steps stored in 'enode.out' is    121.
The tip position is  0.16032180E+01 m.
Appropriate variables are stored in the file 'nextrun.out' for ulterior runs
 starting from the state reached so far. For ulterior runs, the file 'nextrun.out'
will have to be copied to or renamed ''restart.inp'.

Do you want to create a file with the tip position as a function of time [1 for
yes, 0 for no].  0

Do you want to create a file with the void ratio distribution at a given time [1
for yes, 0 for no].  0
```

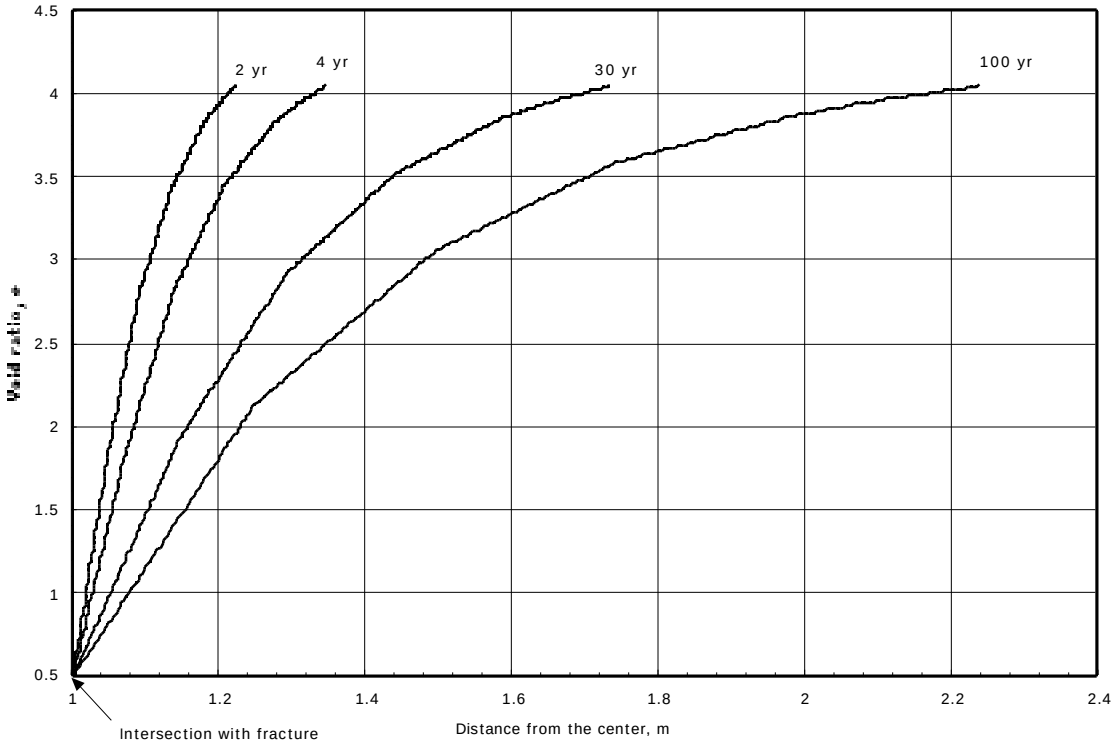
4.5
4
3.5
3
2.5
2
1.5
1
0.5
Void ratio, e
2 yr
4 yr
30 yr
100 yr
1
1.2
1.4
1.6
1.8
2
2.2
2.4
Intersection with fracture
Distance from the center, m